

UNIVERSITY OF KWAZULU-NATAL

**Calibration Techniques for 21-cm
Experiments with Application to HERA:
Quasi-Redundant Calibration Analysis**

by

Mthokozisi Sibusiso Mdlalose

Submitted in fulfillment of the
academic requirements for the degree of
Master of Science,
in the
School of Chemistry and Physics
University of KwaZulu-Natal

Durban

February 2018

*You learn how to cut down trees by cutting them down.
Bateke proverb*

Abstract

Upcoming 21 cm observations promise to open a new window in our understanding of the universe from the epoch of recombination down to redshift of $z \sim 1$. However, measurements of 21 cm signals come at a high cost since the 21 cm signals are buried under galactic and extragalactic foregrounds that are 4 to 5 orders of magnitude brighter. To overcome this challenge, instruments with high sensitivity and large fields of view are required to detect 21 cm signals. Furthermore, robust techniques are required to perform high precision calibration and foreground removal. Studies have shown that per-frequency antenna gain calibration errors of 1 part 10^3 will easily swamp the desired signal if an incomplete point source catalogue is used in calibrating the 21 cm instruments. To enhance sensitivity and lower the computational cost, the design and construction of a new generation of 21 cm instruments characterized by maximally redundant array configuration has been undertaken. The Donald C. Backer Precision Array for Probing the Epoch of Reionization (PAPER) has been successfully calibrated using redundancy in an array configuration, which assumes that in a perfect redundant array, nominally identical baselines measure the same sky signal. In this work, we show that imperfectly redundant arrays produce per-frequency antenna gain calibration errors that can swamp the 21 cm power spectrum measurement. For a test case done using the observed antenna gain auto-correlations from early HERA data, applying correlation calibration in a way that accounts for primary beam variations

in the array improves the per-frequency antenna gain amplitude and phase residuals by a factor of 11.4 and 2159 over the redundant calibration for 5% noise level in primary beam variations adopted in simulations. Including 30 bright sources with known positions, significantly improves the per-frequency antenna gain amplitude and phase calibration errors by a factor of 16 and 2317 respectively over redundant calibration. The flexibility of correlation calibration will play a significant role in quantifying and mitigating the per-frequency antenna gain calibration errors that can make 21 cm power spectrum reconstruction impossible. Furthermore, correlation calibration will be useful in solving for instrumental parameters of 21-cm instruments such as Hydrogen Epoch of Reionization Array (HERA), Hydrogen Intensity and Real-time Analysis eXperiment (HIRAX), Canada Hydrogen Intensity Mapping Experiment (CHIME), The Tianlai project and SKA-low.

Preface and Declaration

The work described in this dissertation was carried out in the School of Mathematical Sciences, University of KwaZulu-Natal, Durban, from August 2015 to October 2017, under the supervision of Prof Jonathan Sievers .

These studies represent original work by the author and have not otherwise been submitted in any form for any degree or diploma to any tertiary institution. Where use has been made of the work of others it is duly acknowledged in the text.

Mthokozisi Sibusiso Mdlalose

February 2018

Acknowledgments

Firstly, I would like to thank my family and friends for supporting me throughout my Masters program. Secondly, I would like to thank my supervisor Prof Jonathan Sievers for his support and guidance through my research. Furthermore, I would like to thank him for organizing exchange programs to University of Pennsylvania, USA and University of Toronto, Canada. I would also like to appreciate the hosting supervisors from each university, Prof James Aguirre, University of Pennsylvania and Prof Keith Vanderline, University of Toronto.

Thirdly, I would to thank SKA-SA, Masters 2015 SKA Scholarship and University of KwaZulu-Natal, 2016 Talent Equity Scholarship for funding my studies. Lastly, ngithanda ukubonga uMveli-nqga-ngqi ngokunika amandla nokubekezela.

Contents

Abstract	ii
Preface and declaration	iii
Acknowledgments	iv
Contents	v
List of Tables	vii
List of Figures	viii
1 Introduction	1
2 21 cm Cosmology	6
2.1 21 cm line Spin Temperature	6
2.2 First Stars and Galaxies	9
2.3 21 cm Power Spectrum Measurement	10
3 Traditional Calibration	15
3.1 Basics of Interferometry	15

3.2	Traditional Calibration	16
3.2.1	Point Source Calibration	18
4	Redundant Baseline Calibration	21
4.1	Redundant Baseline Calibration Formalism	21
4.2	Logarithmic and Linear Redundant Baseline Calibration	24
4.3	Newton Multivariate Method Formulation	26
4.3.1	Gradient and Curvature Test	27
4.4	Results and Discussion	30
4.4.1	Simulation	31
4.4.2	Calibration Errors for Redundant Array	32
4.4.3	Quasi-Redundant Array Simulations	36
5	Correlation Calibration	46
5.1	Introduction	46
5.2	Correlation Calibration	48
5.2.1	Correlation of Visibility	50
5.2.2	χ^2 Minimization	53
5.3	Correlation Calibration Simulations	53
6	Conclusion	60
	Bibliography	61

List of Tables

List of Figures

1.1	21-cm instruments. a) PAPER-128 telescope at SKA site, Karoo, South Africa. ¹	
	b) HERA-19 Telescope and behind it, it PAPER-128 telescope. ²	2
1.2	21-cm instruments. a) Chime Telescope at Dominion Radio Astrophysical Observatory (DRAO) near Penticton, British Columbia, Canada. ³ b) Artist's conception of the HIRAX telescope which is currently under construction and will be deployed in 2018/19 in the South African Karoo, near the SKA site. ⁴	3
2.1	The hyperfine splitting of $1S$ state of hydrogen atom. ⁵	7
2.2	The evolution of 21 cm signal. The top plot demonstrates the history of structure formation as a function of redshift. The bottom plot displays the evolution of 21 cm brightness temperature as a function of frequency at different epoch (Pritchard & Loeb, 2012).	10

¹<http://eor.berkeley.edu/>

²<http://reionization.org/>

³<http://chime.phas.ubc.ca/>

⁴<http://www.acru.ukzn.ac.za/hirax/>

⁵<https://www.skatelescope.org/radio-astronomy/>

2.3	A plot of evolution of power spectrum fluctuations as function z at different slices of k , for $k = 0.01, 0.1, 1, 10 \text{ Mpc}^{-1}$. Different curves show $P(k,z)$ as function of redshift z at fixed k for. Diagonal lines displays $\epsilon T_{fg}(\nu)$, the foreground temperature reduced by a factor ranging from 10^{-3} - 10^{-9} indicate the level of foreground removal required to detect the signal (Pritchard & Loeb, 2012). EoR power spectrum detection requires 10^{-5} level of foreground mitigation.	12
2.4	A plot of 21 cm dimensionless power spectrum $\Delta^2 k$ at $k = 0.2 \text{ h Mpc}^{-1}$ for different heating and reionization models (red, orange and brown). For a 1σ thermal noise errors on $\Delta^2 k$ with 1080 hr of integration, telescope sensitivity as function of redshift for different 21 cm instruments is shown, in which HERA-350 has highest sensitivity (black) DeBoer et al. (2017)	13
2.5	A plot of 2D power spectrum (PS) obtained from a traditional per-frequency antenna calibration methods (left) with incomplete source catalogue, a reference 2D PS without simulated calibration effects (middle) and their difference 2D PS (right). On the residual plot (right), red indicates a relative excess of power, and blue indicates a relative depression of power. Spectral contamination power at all modes in the EoR window is evident. The most sensitive, theoretically contaminant-free EoR modes have excess power on levels of $10^7 \text{ mK}^2 \text{ h}^{-3} \text{ Mpc}^3$, when per-frequency antenna calibration errors are 10^3 order of magnitude, making the measurement impossible (Barry et al., 2016).	14
3.1	(Cornwell, 2004) describe the above example of a two element radio interferometry as \mathbf{b}_λ is baseline vector, σ is angular distance between the position s of source in the sky and the phase centre position s_0 , of the interferometry.”	17
4.1	Antenna positions for a 3×3 array. Labels 0-8 are antenna indices. For an example baselines 0-1, 1-2,3-4, 4-5, 6-7 and 7-8 all have the same length and orientation, these form a unique redundant set 1. In total there are 12 unique sets of redundant baselines. Each colour represents a unique redundant baseline set.	22

4.2	A Plot of χ^2 true, χ^2 predicted from second-order approximation and residuals between true and predicted χ^2 for both real and imaginary part of antenna gain. From the two above plots the second-order approximation of χ^2 predict true χ^2 when we vary one parameter, antenna gain (ant7), fixing other parameters. The size of residuals between true and predicted χ^2 are 10^{-20}	28
4.3	A Plot of χ^2 true, χ^2 predicted from second-order approximation and residuals between true and predicted χ^2 (log scale) for both real (top) and imaginary (bottom) part of true visibility. From the two above plots the second-order approximation of χ^2 predict true χ^2 when we vary one parameter, a true sky visibility V_8 (from an 8th set of unique true sky visibility) , fixing other parameters. The size of residuals between true and predicted χ^2 are about 10^{-20}	29
4.4	<i>Top</i> :A 8×8 HERA like antenna array, located at SKA site, Karroo, South Africa. We pick a representative phase centre to be at (21.4278,-30.7224) deg. <i>Bottom</i> : Gaussian primary beam pattern with a Full-Width-Half-Maximum of 7 deg.	33
4.5	<i>Top</i> : A scatter plot of antenna gain amplitude residual for 64 antennas at 170-230 MHz. <i>Bottom</i> : A scatter plot of phase residual at for all 64 antennas at 170-230 MHz. An optimum solution is reached after 10 iterations with the average amplitude/phase calibration errors across all antennas and frequency, 0.5×10^{-11} and 0.13×10^{-11} respectively. Each colour represents the antenna gain residuals from each individual antenna.	34
4.6	<i>Top</i> :A plot of true visibilities (red dots) and best fit visibilities (blue stars) on the complex plane at 170 MHz. With a cut-off χ^2 of 10^{-20} , an optimum solution is reach after 10 iteration with significantly small residuals of order 10^{-11} and 10^{-19} for real and imaginary components respectively, see the bottom plot of Figure 5.5.	35

4.7	<i>Top</i> : A plot of gain amplitude auto-correlations as function of frequency for three HERA antennas (10,11,73) at different times . At Galactic Center. <i>Bottom</i> : A plot of gain amplitude auto-correlations as function of frequency for three antennas (10,11,73) at high latitude. Data is from HERA19, [courtesy of HERA/Christ Carilli].	38
4.8	<i>Top</i> : A plot of ϵ as function of frequency for all 64 antennas. Here ϵ is primary beam variation. <i>Bottom</i> : A plot of a product of beam responses from antenna 1 and 2 as function θ in radians for i) identical primary beams, $\epsilon_1 = \epsilon_2 = 0$ (blue curve) and , ii) $\epsilon_1 = 0.0664$ and $\epsilon_2 = 0.0520$ (green curve). There is significant difference in power response between a case of identical primary and 5% beam variations in range of 0.01 – 0.10 radians.	39
4.9	<i>Top</i> : A plot of gain amplitude calibration solution as functions of frequency. <i>Bottom</i> : A plot of gain phase as function frequency. The amplitude/phase calibration errors are $\sim 10^{-2}/10^{-3}$ and highly correlated between frequencies. Each colour represents amplitude/phase residuals for each antenna, with a total of 64 antennas.	41
4.10	A plot of true visibilities (red dots) and best fit visibilities (blue stars) on the complex plane at 170 MHz. With optimum solution after 10 iterations, $\chi^2 = 10^{-20}$	42
4.11	A plot of gain amplitude auto-correlation as functions of frequency. At optimum solution amplitude calibration error is 3.7×10^{-12}	43
4.12	A plot of gain phase auto-correlation as functions of frequency. At optimum solution amplitude calibration error is 2.2×10^{-12}	44
4.13	A plot of gain amplitude auto-correlation as functions of frequency. At optimum solution amplitude calibration error is 1.6×10^{-2}	44
4.14	A plot of gain phase auto-correlation as functions of frequency. At optimum solution amplitude calibration error is 9.5×10^{-3}	45

5.1	<i>Top</i> : A plot of gain amplitude calibration solution as functions of frequency without source treatment. <i>Bottom</i> : A plot of gain amplitude calibration solution as function frequency. The calibration errors without/with source treatment in covariance are 1.4×10^{-3} and 1.0×10^{-3}	55
5.2	<i>Top</i> : A plot of gain phase calibration solution as functions of frequency without source treatment. <i>Bottom</i> : A plot of gain phase calibration solution as function frequency. The calibration errors without/with source treatment in covariance are 4.40×10^{-6} and 4.0×10^{-6}	56
5.3	<i>Top</i> : A plot of lincal (blue curve), corrcal (green curve) and corrcal + bright sources (red curve) gain amplitude auto-correlation as functions of frequency. <i>Bottom</i> : A plot of corrcal (green curve) and corrcal + bright sources (red curve) gain amplitude auto-correlation as functions of frequency. Without a bright source treatment, the calibration errors reduced significantly reduced by a factor of 11.4 and for 30 bright source treatment, it improved by a factor of 16. . . .	58
5.4	<i>Top</i> : A plot of lincal (blue curve), corrcal (green curve) and corrcal + bright sources (red curve) gain phase auto-correlation as functions of frequency. <i>Bottom</i> : A plot of corrcal (green curve) and corrcal + bright sources (red curve) phase auto-correlation as functions of frequency. Without a bright source treatment, the calibration errors reduced significantly reduced by a factor of 2159 and with bright source included, phase calibration errors reduced by 2317	59

CHAPTER 1

Introduction

Despite the great progress that has been made in understanding cosmology, the history of the universe between recombination and the redshift of $z \sim 6$ is almost unconstrained observationally. Observations of the 21 cm line from neutral hydrogen (HI) promise to open a new window in cosmology to study structure formation at high redshift and to help constrain cosmological parameters (Furlanetto et al., 2006). However, the 21 cm signal from high redshifts is very weak compared to the foreground signals, which can be 4 to 5 orders of magnitude brighter. In addition to foregrounds, the Earth's atmosphere (particularly the ionosphere) and instrumental systematics can contaminate the 21 cm signal. These challenges for high-redshift 21-cm observations require robust techniques to perform a high precision calibration and to remove foregrounds from the 21 cm signal. A new generation of instruments with high sensitivity and large fields of view is required to meet such demands for 21 cm observations. 21 cm instruments such as the Precision Array to Probe the Epoch of Re-ionization (PAPER) (Ali et al., 2015) and the upcoming instruments such as Hydrogen Epoch of Reionization Array (HERA) (DeBoer et al., 2017), the Hydrogen Intensity and Real-time Analysis eXperiment (HIRAX) (Newburgh et al., 2016), the Canadian Hydrogen Intensity Mapping Experiment (CHIME) (Bandura et al., 2014) and The

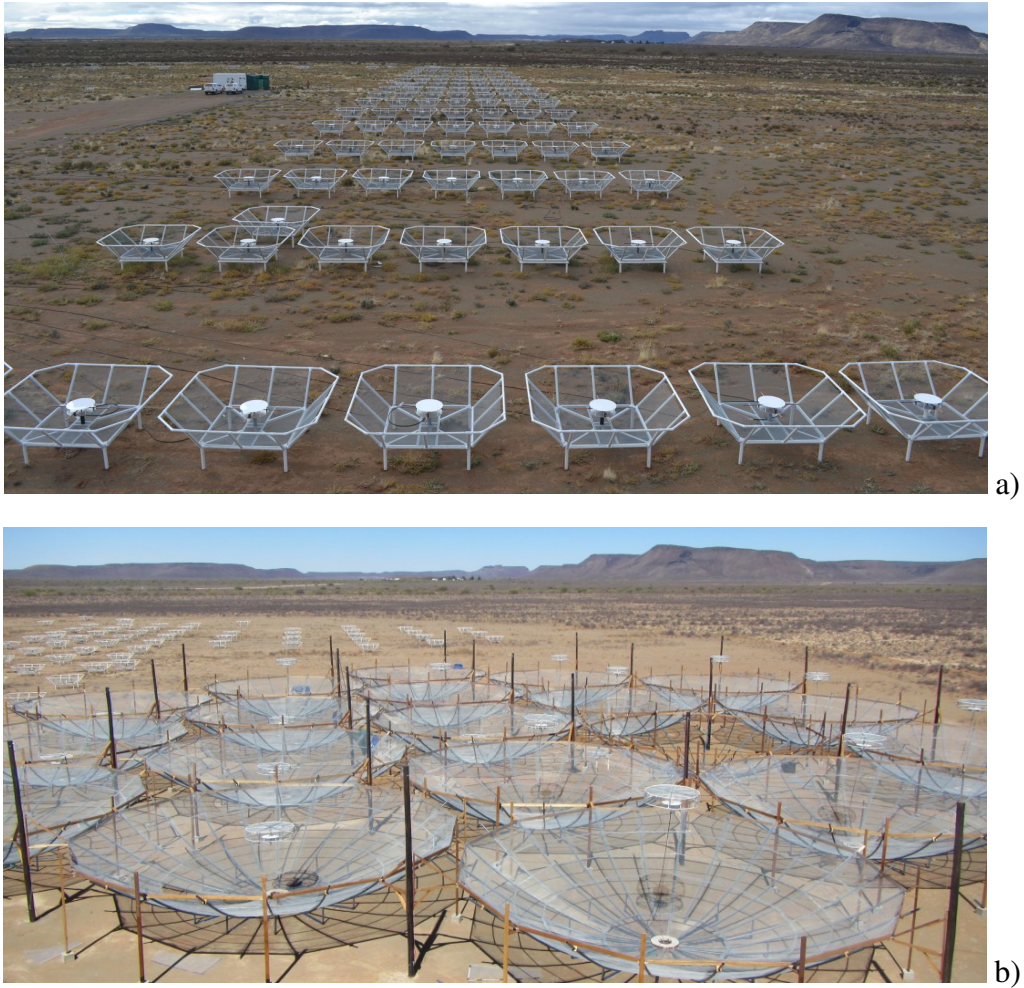


Figure 1.1: 21-cm instruments. a) PAPER-128 telescope at SKA site, Karoo, South Africa.³ b) HERA-19 Telescope and behind it, it PAPER-128 telescope.⁴

Tianlai project (Chen, 2012) are designed to meet 21 cm signal detection requirements, see Figures 1.1 and 1.2. These instruments are generically laid out in redundant arrays, with the same baseline measured by many pairs of antennas. The redundant array configuration in these upcoming 21 cm instruments meets the criteria of high sensitivity over large scales, which is essential in computing statistical measurements of 21 cm signal. Furthermore, the redundant feature makes the calibration analysis more computationally efficient, since these instruments have 100 -1000 elements.

The 21 cm signal is dominated by diffuse galactic emission along with extra-galactic bright



Figure 1.2: 21-cm instruments. a) Chime Telescope at Dominion Radio Astrophysical Observatory (DRAO) near Penticton, British Columbia, Canada.⁷b) Artist's conception of the Hirax telescope which is currently under construction and will be deployed in 2018/19 in the South African Karoo, near the SKA site.⁸

radio sources, so constructing a sensible sky model with the necessary quality is challenging for traditional calibration schemes such as self-calibration (Cornwell, 2004). This is because an algorithm such as CLEAN (Cornwell, 1986; N. OOZEER, 2014) used in self-calibration, traditionally requires a sufficient number of point-like source/s in the initial sky model to give a sensible calibration solution. In the limit of a Gaussian random field sky, in Fourier space each uv point is independent. So, there is no correlation between visibilities that do not overlap in uv space. Therefore, there is no sensible structure in UV-space that spans across all uv points for a diffuse signal. Self-calibration is a powerful tool, but its power ceases in this instance. An alternative approach is to do self-calibration in UV-space.

In traditional redundant baseline calibration (Liu et al., 2010), the sky model is just a single value at each uv point, and a set of visibilities at unique uv points are assigned a single sky value. This is based on the assumption that the same baselines with identical primary beams measure the same sky value. Redundant baseline calibration has been applied in power spectrum reconstruction analysis in one of the 21 cm instrument pathfinders, PAPER (Ali et al., 2015; Ali et al., 2015). In the redundant baseline calibration scheme, the sky is measured at the distinct uv points where the number of distinct uv points is much less than the total visibility points. The values for the antenna-based gains and the sky at these distinct uv points are solved for simultaneously. In the case of a perfectly redundant array, with no prior knowledge of the sky, redundant baseline calibration solutions are optimal. Unfortunately, in real life, imperfections in antenna arrays such as those due to the variations in antenna primary beams and antenna positions will break perfect redundancy. Such instrumental systematics have the potential to produce calibration errors that will swamp the desired 21 cm signal. Barry et al. (2016), for instance, illustrates that 1 part in 10^3 per-frequency antenna calibration errors due the incompleteness of the calibration catalogue introduce excess power in the Epoch of Reionization (EoR) Power Spectrum (PS) measurement, making the detection of EoR signal impossible. Therefore, quasi-redundancy in an array must be accounted for in the calibration analysis. In this work, we focus on determining the level of calibration errors produced by variations due to antenna primary beams variations. Furthermore, we explore how we can reduce those calibration errors using an alternative calibration technique that can account for the variations in the primary beams, called correlation calibration (Sievers,

2017). This work is arranged as follows: in Chapter Two, we discuss 21-cm cosmology and recent results on 21 power spectrum measurements. Basic interferometry and different calibration techniques are discussed in Chapter Three. In Chapter Four, we review redundant baseline calibration and present calibration analysis from simulations. In Chapter Five, we briefly review correlation calibration method and apply correlation calibration to simulations. In Chapter Six, we conclude by highlighting our findings, their implications, and discuss future research ideas.

CHAPTER 2

21 cm Cosmology

Our universe contains a large amount of atomic hydrogen present in the intergalactic medium (IGM) at high redshift. Hence, hydrogen serves as a convenient tracer of the properties of the gas in the history of the universe. Our focus is on the 21 cm line, which is produced by the hyperfine splitting of the $1S$ due to the interaction of the magnetic moments of the proton and of the electron (Pritchard & Loeb, 2012). This process leads to two distinct levels with an energy difference $\Delta(E) = 5.9 \times 10^{-6} eV$, which corresponds to a frequency of 1420 MHz or a wavelength of 21.1 cm, see 2.1 ¹. In the following section, we briefly review basic concept of 21 cm line Spin Temperature, details are discussed in Field (1959).

2.1 21 cm line Spin Temperature

The hyperfine state of 21 cm line has two levels: singlet (ground state) and triplet (excited state) states. Singlet and triplet states have angular momentum F values of $F = 0$ and $F = 1$ respectively. In a triplet state, orientation between electron and proton magnetic moment is parallel.

¹<http://skatelescope.org/radio-astronomy/>

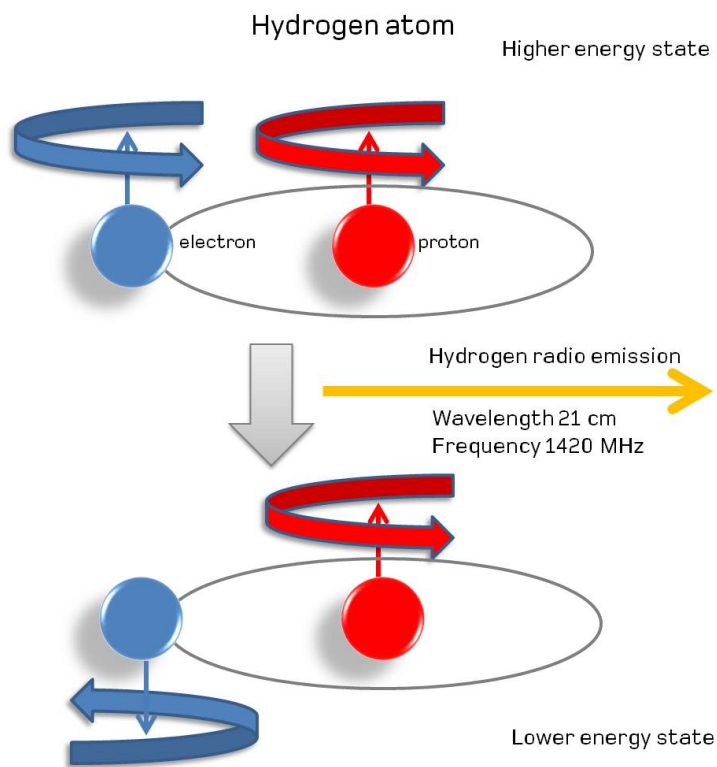


Figure 2.1: The hyperfine splitting of $1S$ state of hydrogen atom.²

And a ground is an anti-parallel orientation between electron and proton magnetic moment. The de-excitation from triplet state to singlet state result into an anti-parallel orientation, this termed a 'spin-flip' and 21 cm radiation is emitted. In a spontaneous transition, a lifetime of de-excitation (from triplet state to singlet state) and excitation (from singlet state to triplet state) is 1.1×10^7 years. Such a long lifetime makes the background radiation and collisions in hydrogen gas cloud important in studying the evolution of 21 cm line. A beam of 21 cm radiation passing through a hydrogen cloud, results in absorption and induced emission of 21 cm radiation. If the hydrogen cloud were in thermodynamic equilibrium at T , a hydrogen Spin temperature T_S is equal to thermodynamic temperature if the gas is in the thermal equilibrium, then according to Boltzmann's law, ratio of number of electrons in an excited versus ground state is

$$n_1/n_0 = g_1/g_0 \exp(-h\nu_{10}/kT_S) \quad (2.1)$$

where $g_1 = 3$ and $g_0 = 1$ are statistical weights of the upper triplet state and lower singlet state respectively. h is Planck constant and k is Boltzmann constant. T_S is set by dynamical processes in hydrogen cloud. If the dynamic process is dominated by collisions with associated the kinetic temperature T_k , then $T_S \rightarrow T_k$ or $T_S \rightarrow T_{CMB}$ or $T_S > T_{CMB}$, where T_{CMB} is Cosmic Micro-background temperature. 21-cm instruments measures a redshifted 21 cm line, $\nu_{21cm}(z) = \nu_{21cm}/(z + 1)$, where is a $\nu_{21cm}(z)$ is frequency of 21 cm line at redshift z .

Qualitatively, we understand the evolution of T_S at different z given the standard of cosmological model (Pritchard & Loeb, 2012). At the surface of last scatter, $z \approx 1000$, $T_S = T_K = T_{CMB}$ and just after the last scatter, $T_S = T_K$. In the adiabatic expansion $T_k \propto a^{-2}$ and $T_{CMB} \propto a^{-1}$, where a is expansion scale factor. An epoch when $T_S = T_K < T_{CMB}$ is called Dark ages. A time goes by after the CMB last scatter, T_k drop fast that T_{CMB} as the universe is expanding with a scale factor a . When the time scale to absorb a photon is short than the time scale of atomic hydrogen to loss temperature physical through collisions, the absorption of CMB photons by hydrogen cloud starts and eventually, $T_S \rightarrow T_{CMB}$.

After millions of years after recombination, over-dense regions start to collapse under gravity, when their reach critical temperatures to start nuclei fusion reaction, first stars are formed and then galaxies.. The 100 of times repeated absorption and re-emission of Ly α photons (from first

stars and galaxies) by neutral hydrogen gas, this process couples T_S to T_k . This process is called Wouthuysen-Field Effect (Pritchard & Loeb, 2012). As the universe expands, T_k goes below T_{CMB} while neutral hydrogen gas absorbed Ly α and CMB photons at a fast rate. Eventually, the energy output heats the gas again, so that $T_k > T_{CMB}$ and the gas is still coupled to T_k , therefore $T_S > T_{CMB}$ and 21 cm radiation emission starts around $z \sim 15$. This epoch is called Epoch of Reionization (EoR).

Quantitatively, to study the evolution of the 21 cm, we look at the evolution of an observable differential brightness temperature T_b due to the redshifted 21-cm signal from a cloud of hydrogen gas in the IGM (Ali et al., 2015):

$$\delta T_b(z) \approx 27(1 + \delta)x_{HI} \left(1 - \frac{T_{CMB}}{T_S}\right) \left(\frac{1+z}{10}\right)^{1/2} mK \quad (2.2)$$

δ is the local matter over-density of the gas, x_{HI} is the neutral fraction of the gas. Equation (2.2) tells us that we observe δT_b when $T_S \neq T_\gamma$. Figure 2.2 displays the evolution of the sky-averaged 21 cm signal as a function of redshift. The top plot demonstrates the history of hydrogen ionization as a function of redshift. The bottom plot displays the evolution of 21 cm brightness temperature as a function of frequency at different epochs. At high redshift $z \sim 1000 - 50$, there is a high amount of neutral hydrogen. About $z \sim 40 - 30$, the formation of first stars and galaxies occurs leading to the first hydrogen ionization (Pritchard & Loeb, 2012). Absorption of Ly α photons and CMB photons by hydrogen gas in IGM around $z \sim 30 - 18$. The epoch of Reionization occurs around $z \sim 18 - 7$. Hydrogen gas in IGM is almost completely ionized from $z \sim 6$ up to today ($z = 0$) Furlanetto et al. (2006). In following section, we briefly discuss how we can learn about the formation of first stars and galaxies from EoR signal.

2.2 First Stars and Galaxies

After the dark ages, areas of higher-gas density inside dark matter halos began to collapse under gravity, and the neutral gas in the universe began clump together. After sometime, these regions continue to collapse until they reach high temperatures to start igniting nuclear fusion in their

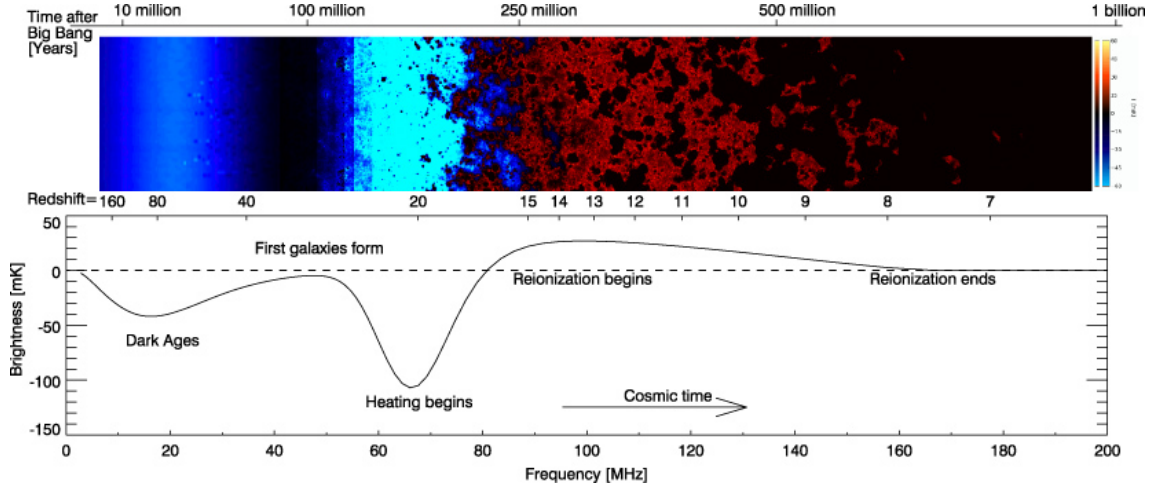


Figure 2.2: The evolution of 21 cm signal. The top plot demonstrates the history of structure formation as a function of redshift. The bottom plot displays the evolution of 21 cm brightness temperature as a function of frequency at different epoch (Pritchard & Loeb, 2012).

cores and leading to the first stars and galaxies. The high energy light from these newly formed stars start to ionize the neutral hydrogen gas around them, forming small bubbles of ionized gas. As these bubbles grew and punched ever-larger holes into the neutral universe, they eventually began to overlap, enabling ionizing radiation to travel farther and farther through space. Cosmologists believe that the primordial stars and galaxies are primary sourcing for the Epoch of Reionization of neutral hydrogen gas in IGM. 21 cm power spectrum measurement will help to put constraints on the EoR period, Δz and the evolution HI cloud during EoR (Norman, 2016). To do this amazing science with the 21-cm signal, astronomers need to solve the two main problems which are; foregrounds removal and high precision calibration of 21-cm data from the 21 cm instrument. In the following section we briefly review recent results on 21 cm Power Spectrum measurement.

2.3 21 cm Power Spectrum Measurement

In the previous sections, we reviewed different component of 21 cm average temperature as function of redshift. 21 cm signal can be studied statistical through Power Spectrum (PS) anal-

ysis. 21 cm PS is measured in three-dimensions, two angular dimensions and one frequency dimension. Figure 2.3 shows the expected 21 cm power spectrum temperature fluctuations as a function of redshift at different scale $|\mathbf{k}|$ in Mpc^{-1} (Pritchard & Loeb, 2012), $|\mathbf{k}|$ is length of a wavenumber $\mathbf{k} = (k_x, k_y, k_z)$. Diagonal lines in Figure 2.3 tells us about the required effort to remove foreground and sensitivity to detect 21 cm power spectrum in different redshift epoch. About 10^{-5} level sensitivity in foreground required to be mitigated in order to detect EoR signal. Figure 2.4 compares 21 cm telescopes sensitivities as a function of redshift to models of the evolving, dimensionless power spectrum parameter $\Delta^2 k = k^3 P(K)/2\pi^2$ at $k = 0.2 h Mpc^{-1}$ (DeBoer et al., 2017). In Figure 2.4, we note that the sensitivity of *HERA* – 350 (350 dish elements) is expected to high then the current 21 cm telescopes. Furthermore, *HERA* – 350 will be able to measure EoR with high a precision. A recent study on 21 cm EoR power spectrum analysis reveals that simulation values of the intrinsic foregrounds of $10^{14} mK^2 h^{-3} Mpc^3$ and per-frequency antenna amplitude deviations of about 10^{-3} introduce excess power of $10^7 mK^2 h^{-3} Mpc^3$ into Epoch of Reionization window (Barry et al., 2016). Figure 2.5 shows the power spectrum (PS) as a function of modes perpendicular to the line-of-sight (k_{\perp}) and modes parallel to the line-of-sight (k_{\parallel}) for an incomplete source catalogue (far left), complete source catalogue (middle) and the residual (far right). Axes are displayed in units of Hubble constant (h) times inverse megaparsec (Mpc^{-1})” as described in Barry et al. (2016). In general, any instrumental systematic that leads to calibration errors of 1 part 10^3 has a potential introduce excess power in Epoch of Reionization window. We desire to determine the size of calibration errors due to variations in antenna’s primary beams. Furthermore, we look at calibration techniques to reduce the calibration errors to a level below the targeted EoR detection. The next chapter is dedicated to discussing the basic interferometer and brief review of traditional calibration techniques.

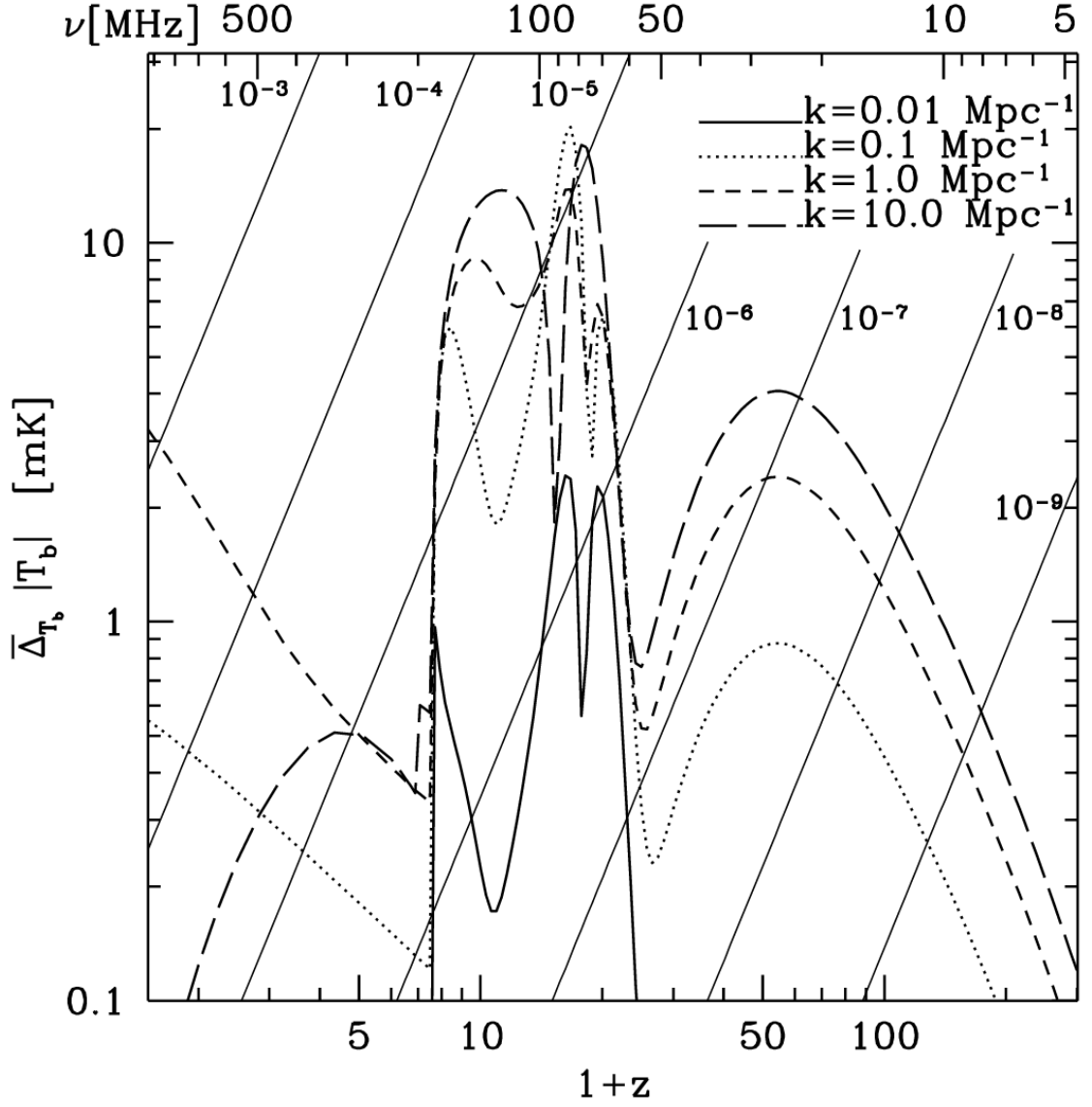


Figure 2.3: A plot of evolution of power spectrum fluctuations as function z at different slices of k , for $k = 0.01, 0.1, 1, 10 \text{ Mpc}^{-1}$. Different curves show $P(k, z)$ as function of redshift z at fixed k for. Diagonal lines displays $\epsilon T_{fg}(\nu)$, the foreground temperature reduced by a factor ranging from 10^{-3} - 10^{-9} indicate the level of foreground removal required to detect the signal (Pritchard & Loeb, 2012). EoR power spectrum detection requires 10^{-5} level of foreground mitigation.

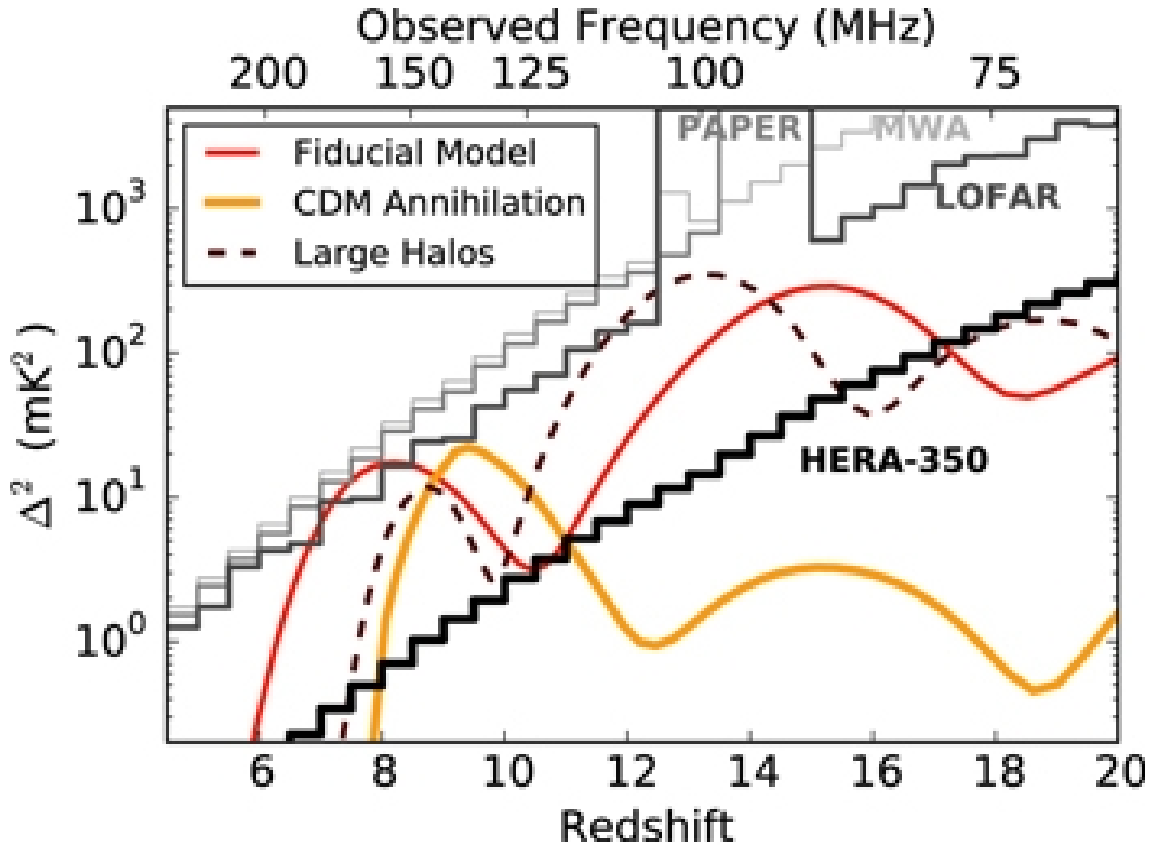


Figure 2.4: A plot of 21 cm dimensionless power spectrum $\Delta^2 k$ at $k = 0.2 h Mpc^{-1}$ for different heating and reionization models (red, orange and brown). For a 1σ thermal noise errors on $\Delta^2 k$ with 1080 hr of integration, telescope sensitivity as function of redshift for different 21 cm instruments is shown, in which HERA-350 has highest sensitivity (black) DeBoer et al. (2017)

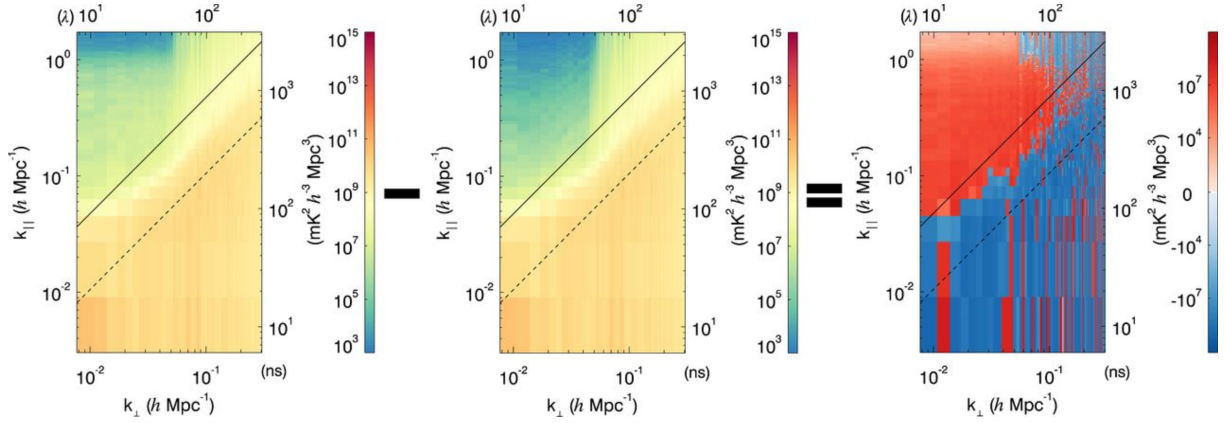


Figure 2.5: A plot of 2D power spectrum (PS) obtained from a traditional per-frequency antenna calibration methods (left) with incomplete source catalogue, a reference 2D PS without simulated calibration effects (middle) and their difference 2D PS (right). On the residual plot (right), red indicates a relative excess of power, and blue indicates a relative depression of power. Spectral contamination power at all modes in the EoR window is evident. The most sensitive, theoretically contaminant-free EoR modes have excess power on levels of $10^7 \text{ mK}^2 h^{-3} \text{ Mpc}^3$, when per-frequency antenna calibration errors are 10^3 order of magnitude, making the measurement impossible (Barry et al., 2016).

CHAPTER 3

Traditional Calibration

To understand the how to calibrate the 21 cm observations; in this chapter we review the basics of interferometry and traditional calibration.

3.1 Basics of Interferometry

The resolution of a single telescope is characterized by $\sim \lambda/D$, where D is dish diameter and λ is a wavelength of observation. For 21-cm observations, we need a telescope with the resolution corresponding to a dish diameter of about 100-1000 meters (Furlanetto et al., 2006). To build such a single dish telescope is highly expensive. An alternative is to use an array of telescopes, which will collectively act as a single telescope. Such a technique is called interferometry. An interferometer measures the correlation of electric field at two different observation locations say, \mathbf{r}_i and \mathbf{r}_q for antennas i and q respectively. Hence, the correlation equation:

$$c_\nu(\mathbf{r}_i, \mathbf{r}_q) = \langle E_\nu^*(\mathbf{r}_i), E_\nu(\mathbf{r}_q) \rangle \quad (3.1)$$

where E_ν is the electric field measured at antennas i and q , at frequency ν . Integrating over the sky, we have

$$c_\nu(\mathbf{r}_i, \mathbf{r}_q) = \int_{\Omega} I_\nu(\mathbf{s}) \exp(-2\pi j \nu \mathbf{b} \cdot \mathbf{s}/c) d\Omega \quad (3.2)$$

where $\mathbf{b} = \mathbf{r}_i - \mathbf{r}_q$ the baseline (the distance between antennas i and q) and s is the vector to a small patch of sky, and $I_\nu(s)$ is the brightness of that patch of sky at frequency ν . In the flat sky approximation, and c_ν becomes the Fourier transform of the intensity $I_\nu(s)$ of source. We redefine a baseline vector as $u = b_x/\lambda$, $v = b_y/\lambda$, $w = \hat{b}_z/\lambda$, measured in wavelengths at the centre of frequency of the observation band, and, in the directions towards East, North and the phase center of the region of interest respectively. The visibility measured by antennas i and q is (N. OOZEER, 2014):

$$V_\nu(u, v, w) = \int_{-\infty}^{+\infty} \int_{-\infty}^{+\infty} A_\nu(l, m) I_\nu(l, m) \exp[-2\pi j \nu (ul + vm + w\sqrt{1 - (l^2 + m^2)})] dl dm / \sqrt{1 - (l^2 + m^2)} \quad (3.3)$$

where l and m are the project coordinate of the sources in the sky. $A_\nu(l, m) = A_{\nu i}(l, m) A_{\nu q}(l, m)$ is a primary beam response measured by antenna i and q . Figure 3.1, shows the example of radio interferometry for two antennas. According to van Cittert-Zenike Theorem, for a spatially incoherence source, the interferometry correlation function 3.1 is equivalent to complex visibility function 3.3, a detail derivation is discussed in Interferometer and Synthesis in Radio Astronomy ¹. The next section will briefly review traditional calibration.

3.2 Traditional Calibration

Calibration can be simply explained as a process of solving the complex correction factors that must be applied to each visibility in order to get as close as possible to a true sky visibility that we would measure, such that the data image gives an accurate picture of the sky. The observed visibility v_{iq} measured by antennas i and q is given by (N. OOZEER, 2014)

$$v_{iq}^{observed} = J_{iq} v_{iq}^{True} \quad (3.4)$$

¹Interferometer and Synthesis in Radio Astronomy by A. Richard Thompson, James M. Moran, and George W. Swenson Jr, chapter 15, 767-781 pg

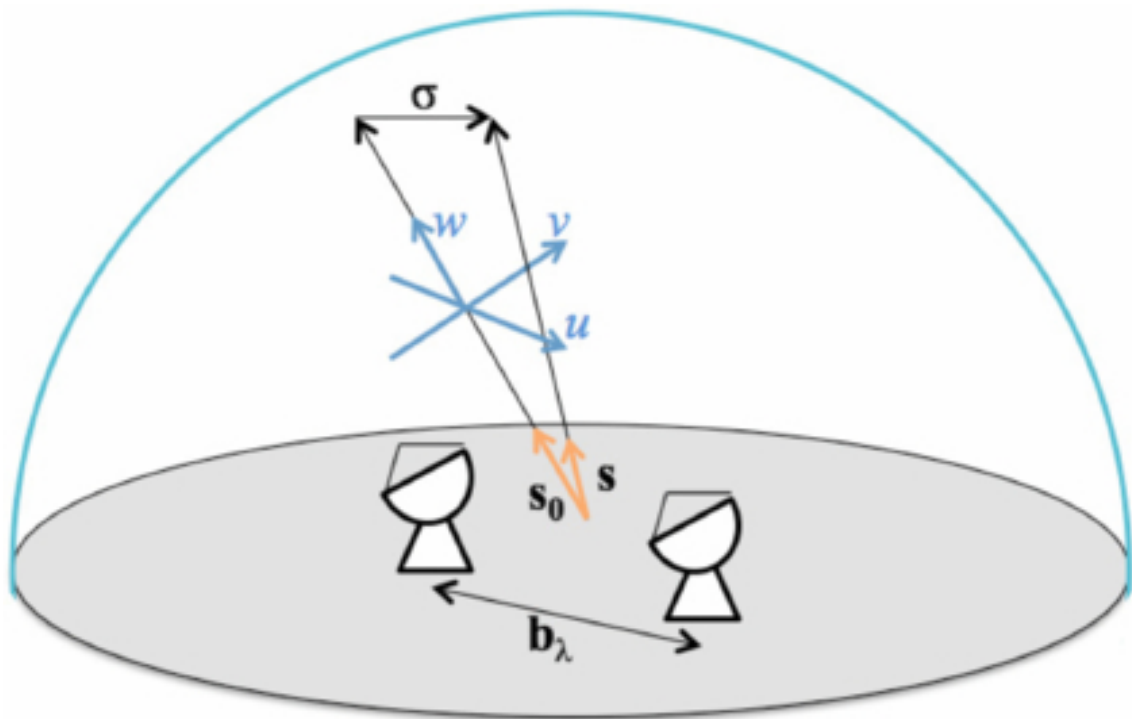


Figure 3.1: (Cornwell, 2004) describe the above example of a two element radio interferometry as \mathbf{b}_λ is baseline vector, σ is angular distance between the position s of source in the sky and the phase centre position s_0 , of the interferometry.”

where J_{iq} represents the accumulation of all complex correction factors affecting visibility measurement on baseline (i, q) and v_{iq}^{True} is a true visibility of the sky . The complex correction factors are due to a signal propagating through atmosphere and ionosphere, interact with gas and get attenuated, through a process called Faraday rotation (Moore et al., 2013). The main object of calibration is to find J_{iq} . Once J_{iq} has been found, we invert it in Equation (3.5), then v_{iq}^{True} is given by:

$$v_{iq}^{True} = J_{iq}^{-1} v_{iq}^{Observed} \quad (3.5)$$

In general, J_{iq} is a function of frequency, polarization and time. Both $v_{iq}^{Observed}$ and J_{iq} are in general complex numbers. We assume that J_{iq} is antenna-based , then J_{iq} we can decompose $J_{iq} = J_i \otimes J_q$. The 2×2 matrixes J_i and J_q are known as Jones matrixes in optical polarimetry and represent the outer product (J.P. Hamaker, 1996). J_i can be further factorized into different factors that affect the radio signal. This factorization is(J.P. Hamaker, 1996)

$$J_i = G_i D_i C_i E_i \quad (3.6)$$

Here G_i, D_i, C_i, E_i represent 2×2 antenna-based gain, leakage terms, nominal feed configuration and parallactic angle rotation In the following section, we review different calibration techniques.

3.2.1 Point Source Calibration

In calibrating a radio telescope, astronomers are mostly interested in these parameters; position (of a source/s in the sky), intensity, and polarization as function of frequency and time. When observing a point source/s, Equation (3.5) becomes

$$v_{iq}^{Observed} = J_{iq} S \quad (3.7)$$

where S is the visibility of a point source of interest. A basic approach to is to use a known bright sources (calibrator/s) near the region of interest to solve J_{iq} 's using least-square algorithm². Thereafter, apply J_{iq} solutions to observation data set, $v_{iq}^{Observed}$. This produce a raw image, S

²Basically, least-squared it a minimization technique that minimizes the sum of squared residual, the difference between an observed value, and the fitted value provided by a model

. This is called point source calibration. This technique works well for resolved point source/s calibration and for small field observations. If a complex object or a large field is observed, standard calibration produces a raw image that is dominated by noise, called a dirty image. Self-calibration is a technique that reconstructs the initial visibility model from the bright point sources in the observed data using an algorithm called CLEAN (Högbom, 1974). CLEAN is way of making a sky image, there are other techniques such Maximum Entropy Method (Cornwell & F. Evans, 1985). For instance in CLEAN algorithm, a clean image of the sky is obtained through an iterative process, where in each step optimum gain solution are applied to the visibility data until the final image is clean. Clean is the one way of making clean image but there other ways such Maximum entropy. Mathematical, a model visibility, v_{iq}^{model} is created iteratively from the observed intensity visibilities, as follows:

$$v_{iq}^{Observed} = J_{iq} v_{iq}^{model} \quad (3.8)$$

Below we quote self-calibration steps as presented in Cornwell (2004):

1. Create an initial source model, typically from a dirty image (or else a point source)
2. Use full resolution information from the clean components or MEM image NOT the re-stored image.
3. Find antenna gains using least squares fit to visibility data
4. Apply gains to correct the observed data.
5. Create a new model from the corrected data. For example, using Clean or Maximum Entropy.
6. Go to step 2, unless current model is satisfactory

Self-calibration has proved to be a useful technique in producing great scientific results such as recent KAT-7 Science verification (Carignan et al., 2013). However, the power of traditional self-calibration ceases when it comes to 21-cm observations. For instance, algorithm such CLEAN (Cornwell, 1986; Högbom, 1974) used in self-calibration scheme, requires sufficient

number of point-like source/s in the initial sky model gives a sensible solution. This mainly because the Fourier Transform of the a point-like source/s is flat in UV-space and it spans all uv points. In the limit where the sky is a Gaussian random field, in Fourier space each uv point is independent, so there are no correlation between uv points that are not overlapping. Hence, there is no sensible structure in uv -space for a diffuse signal. An alternative approach could be to do self-calibration in UV-space. In the next chapter, we discuss an alternative approach called redundant baseline calibration.

Redundant Baseline Calibration

4.1 Redundant Baseline Calibration Formalism

To understand redundant baseline calibration, we reintroduce redundant baseline calibration formalism as discussed in Liu et al. (2010). Suppose antenna i measure a electric field e_i from the sky at a given instant:

$$e_i = g_i x_i + n_i \quad (4.1)$$

where $g_i = e^{(\eta_i + j\phi_i)}$ is complex gain of an antenna (η is amplitude angle and ϕ is the phase angle), x_i is a true electric field and n_i antennas instrumental noise contribution. Assuming that the instrumental noise is uncorrelated with the sky signal and it is antenna based, then correlation of the two signals from two participating antennas is given by:

$$\begin{aligned} c_{iq} &\equiv \langle s_i^* s_q \rangle \\ &= g_i^* g_q \langle x_i^* x_q \rangle + \langle n_i^* n_q \rangle \\ &= g_i^* g_q s_{iq} + n^{res} \end{aligned} \quad (4.2)$$

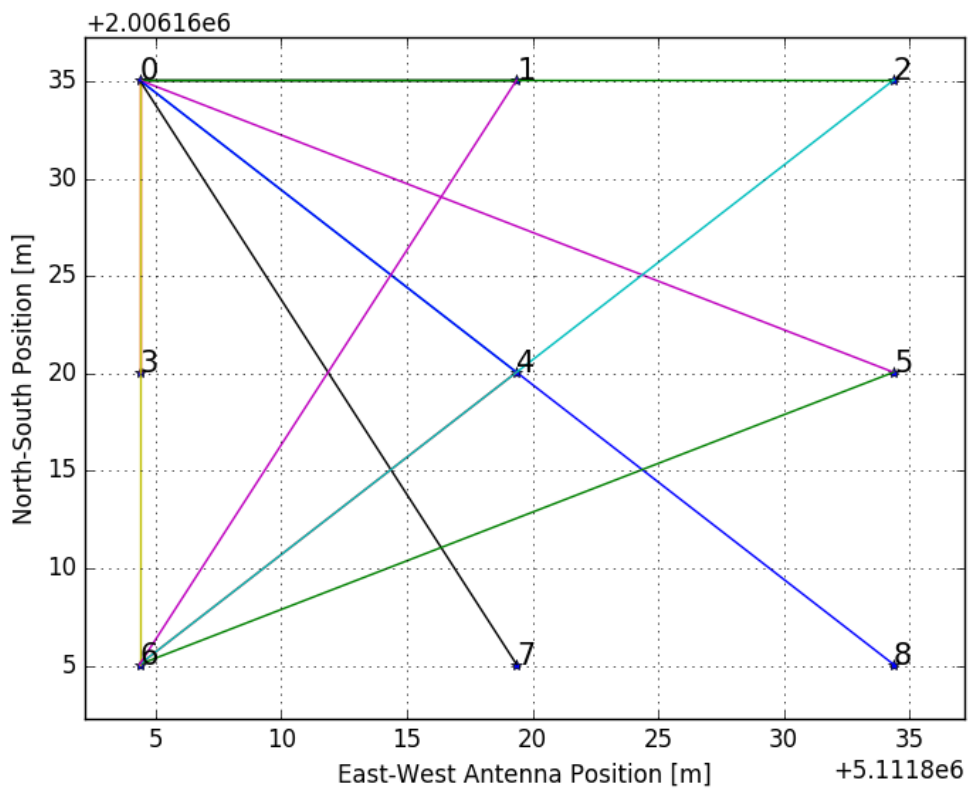


Figure 4.1: Antenna positions for a 3×3 array. Labels 0-8 are antenna indices. For an example baselines 0-1, 1-2,3-4, 4-5, 6-7 and 7-8 all have the same length and orientation, these form a unique redundant set 1. In total there are 12 unique sets of redundant baselines. Each colour represents a unique redundant baseline set.

where s_{iq} is true sky visibility seen by baseline $i - q$ and n^{res} is residual iq noise.

Our main objective is to solve for true correlations s_{iq} from the measured correlations c_{iq} . With N_{ants} number of antennas, an $N_{ants}(N_{ants} - 1)/2$ system of non-linear equations formed in terms of antenna gain amplitude and phase parameters η, ϕ respectively, and the true sky visibility s_{i-q} is unconstrained. This because the number of parameters to solve is greater than the measured correlations. However, if we evoke the power of redundancy in antennas layout, Equation 4.2 becomes over-determined. If an array has a large number of redundant baselines, then the number of unknowns on the right hand side of Equation 4.1 can be reduced by demanding that the true sky visibilities s_{iq} for a set of identical baselines be the same. In each redundant baseline set, we measure one sky value, s_k . The system of Equation 4.2 becomes over-determined, now the task is to solve for N_{ants} antenna gains g_i and approximately $2N_{ants}$ (for a square grid but in general the number of redundant baseline dependants on an array configuration) unique true correlations s_k :

$$c_{iq} = g_i^* g_q s_k + n^{res} \quad (4.3)$$

As an example, let us consider a 3×3 antenna array equally spaced (15 meters apart), see Figure 4.1. From a 3×3 array, we can form 12 unique baselines, and 36 measured correlations. Hence, one must fit for 24 complex numbers (from the true visibilities of the 12 unique baselines) and 9 complex numbers from antenna gains factors from 36 complex measured correlations:

$$\begin{aligned} c_{01} &= g_0^* g_1 s_1 + n_{01} \\ c_{12} &= g_1^* g_2 s_1 + n_{12} \\ &\vdots \\ c_{03} &= g_0^* g_3 s_2 + n_{03} \\ c_{35} &= g_3^* g_5 s_2 + n_{35} \\ &\vdots \\ c_{82} &= g_8^* g_2 s_{12} + n_{82} \end{aligned} \quad (4.4)$$

As a tradition, we omit baselines of length zero. Hence, auto corrections are not considered. In the following sections we introduce two tradition redundant baseline calibration techniques.

4.2 Logarithmic and Linear Redundant Baseline Calibration

There are two traditional techniques to solve for g_i^* , g_q and s_k : Logarithmic Redundant Calibration and Linear Redundant Calibration (Liu et al., 2010). In logarithmic calibration, we take the logarithm of both sides of Equation 4.3 and obtain a decoupled linearized equation in phase and amplitude:

$$\begin{aligned}\ln |c_{iq}| &= \eta_i + \eta_q + \ln |s_k| + \text{Re}w_{iq} \\ \arg |c_{iq}| &= \phi_q - \phi_i + \arg |s_k| + \text{Im}w_{iq}\end{aligned}\quad (4.5)$$

where w_{iq} is weighting noise. We then perform a least squares fit for the system of Equation 4.5, where we solve for η 's, ϕ 's, $\ln |s_k|$ and $\arg |s_k|$:

$$\hat{\mathbf{X}} = (\mathbf{A}^T \mathbf{N}^{-1} \mathbf{A})^{-1} \mathbf{A}^T \mathbf{N}^{-1} \mathbf{d} \quad (4.6)$$

where $\hat{\mathbf{X}}$ least-squared estimator of length m , \mathbf{A} is matrix determined by the array configuration, \mathbf{d} is data from measured correlations and \mathbf{N} is noise covariance matrix. Although logarithmic calibration proves to simplify minimization problem but it comes with two main drawback: Phase wrapping and noise bias. Recovering correct phases of g_i^* , g_q and s_k is challenging if the all antenna phases are not close to zero (Liu et al., 2010). This because logarithmic calibration can not differential between zero radians and the multiplies of 2π . However, amplitudes are correctly recovered since the in system of equations in Equation 4.5, phases and amplitudes decoupled completely. The logarithmic method is not unbiased, in the sense that ensemble averages of noisy simulations do not converge to the true simulated parameter values (Liu et al., 2010).

The logarithm calibration solution are taken initial guess parameters for linearize redundant calibration method. In linearized redundant baseline calibration, as in (Liu et al., 2010) paper, a Taylor expansion of Equation 4.3 around initial estimates g_i^0 , g_q^0 and s_k^0 and a system of linearized equations is:

$$\delta_{iq} \approx \exp(\eta_i^0 + \eta_q^0 - j(\phi_i^0 - \phi_q^0)) [(s_k^1 + s_k^0(\Delta\eta_i + \Delta\eta_q - j(\Delta\phi_i + \Delta\phi_q))] \quad (4.7)$$

where is $\Delta\eta = \eta - \eta_0$ and $\Delta\phi = \phi - \phi_0$. Again performing a least squared fit, we solve for $\Delta\eta$, $\Delta\phi$ and s_k^1 .

All traditional redundant baseline calibration schemes have four degeneracy's; absolute amplitude and phase calibration and phase gradient (x-direction and y-direction). To demonstrate the nature of degeneracy in absolute amplitude and phase, let consider χ^2

$$\sum_{i,q,k} \left(\frac{c_{iq} - g_i^* g_q s_k}{\sigma_{iq}} \right)^2 \quad (4.8)$$

Suppose a new solution is $g'_i = l g_i$, $g'_q = l g_q$ and $s'_k = s_k / l^2$, then $\chi^2(g', s') = \chi^2(g, s)$. This implies that there is direction in which χ^2 is not changing. Physically, this means that we can multiply gain calibration solution by a constant factor and simultaneously divide the sky calibration solution by the same factor. This mathematical degeneracy is due to the sky model Independence of redundant baseline calibration scheme. To remove this degeneracy, we divide gain calibration solution by average gain at each frequency. This gain calibration is crucial step prior to bandpass calibration. The last two additional degeneracies are due to the sky model independence of redundant calibration scheme, the calibration solution is insensitive to tilts of the entire telescope in either the x or the y direction, since such tilts are equivalent to rotations of the sky. To remove this phase gradient degeneracy fit for $\hat{\nabla}\phi$,

$$\hat{\nabla}\phi = (\mathbf{X}^T \mathbf{X})^{-1} \mathbf{X}^T \phi_{sol} \quad (4.9)$$

where \mathbf{X} is an 3-dimension vector of antenna positions and ϕ_{sol} is vector of antenna gain phases from the calibration solution. We compute $\phi_{model} = \hat{\nabla}\phi \mathbf{X}$, therefore $\phi_{correct} = \phi_{model} - \phi_{sol}$. Once all four degeneracies are removed, the next calibration steps follows. In this section, one can see that traditional redundant calibration is self-calibration in UV-space, if the sky model was just a sky values at each uv point and a set of unique uv points are assigned a single sky value. In the next section, we introduce an alternative minimization technique (equivalent to linear redundant baseline method, known as omncal/lincal) for calibrating g_i , g_q and s_k called Newton Multivariate Method.

4.3 Newton Multivariate Method Formulation

When we are calibrating for g_i , g_q and $s_k \equiv s_{i-q}$ (for k is an index of a unique redundant set of true sky visibilities), the minimizing quantity between $N_{ants}(N_{ants} - 1)/2$ measured data points, v_{iq} and the model c_{iq} is

$$\begin{aligned}\chi^2 &= \sum_{i,q}^{N_{ants}(N_{ants}-1)/2} \left(\frac{(v_{iq} - g_i^* g_q s_{i-q})}{\sigma_{ij}} \right)^2 \\ &= (v - c)^T \mathbf{W} (v - c)\end{aligned}\tag{4.10}$$

where σ_{iq} is the measured error for v_{iq} and \mathbf{W} is a diagonal matrix with $W_{iq} = 1/\sigma_{iq}^2$ as diagonal elements, v and c are $(N_{ants}(N_{ants} - 1)/2) \times 1$ column vectors. Since Equation 4.10 is non-linear in model of an m vector of parameters $\mathbf{p} = \mathbf{p}(g, s)$, then the minimization of $\chi^2(\mathbf{p})$ with respect to the parameters will be carried out iteratively. The goal of each iteration is to find a deviation δ to the parameters \mathbf{p} that minimizes $\chi^2(\mathbf{p})$.

To find the parameters δ that give \mathbf{p} which minimizes χ^2 , we approximate Equation 4.10 near \mathbf{p} using a second-order Taylor expansion,

$$\chi^2(\mathbf{p} + \delta) = \chi^2(\mathbf{p}) + \nabla \chi^2(\mathbf{p}) \delta + \frac{1}{2} \delta^T \nabla^2 \chi^2(\mathbf{p}) \delta\tag{4.11}$$

where $\nabla \chi^2(\mathbf{p})$ is given by

$$\begin{aligned}\frac{\partial \chi^2(\mathbf{p})}{\partial \mathbf{p}} &= -2(\mathbf{v} - c(\mathbf{p}))^T \mathbf{W} \frac{\partial}{\partial \mathbf{p}} c(\mathbf{p}) \\ &= -2(\mathbf{v} - c(\mathbf{p}))^T \mathbf{W} \mathbf{J}\end{aligned}\tag{4.12}$$

where \mathbf{J} is $1 \times m$ Jacobian matrix which contains the derivatives of χ^2 with respect to \mathbf{p} . And $\nabla^2 \chi^2(\mathbf{p})$ is given by

$$\begin{aligned}\frac{\partial^2 \chi^2(\mathbf{p})}{\partial \mathbf{p}' \partial \mathbf{p}} &= 2\mathbf{J}^T \mathbf{W} \mathbf{J} \\ &= \mathbf{H}(\mathbf{p})\end{aligned}\tag{4.13}$$

where $\mathbf{H}(\mathbf{p})$ is $m \times m$ Hessian matrix. We want to find δ such that $\frac{\partial \chi^2(\mathbf{p} + \delta)}{\partial \delta} = 0$ where $\mathbf{H}(\mathbf{p})$ is semi-positive definite. This because of four degeneracies discussed in previous section. Now,

Equation 4.11 becomes

$$\frac{\partial \chi^2(\mathbf{p} + \delta)}{\partial \delta} = \nabla \chi^2(\mathbf{p}) + \mathbf{H}(\mathbf{p})\delta \quad (4.14)$$

Therefore, δ

$$\delta = -(\mathbf{H}(\mathbf{p}))^+ \nabla \chi^2(\mathbf{p}) \quad (4.15)$$

We take pseudo inverse $+$, since $\mathbf{H}(\mathbf{p})$ is a singular matrix. A $\mathbf{H}(\mathbf{p}) = U\Lambda V$ where U contains the orthogonal eigenvectors of $\mathbf{H}(\mathbf{p})$ and $U = V^T$ and, Λ is a diagonal matrix that contain the eigenvalues $\mathbf{H}(\mathbf{p})$. In taking a pseudo inverse of $U\Lambda V$, eigenvalues less than 10^{-6} are replaced by zero when taking the inverse of Λ .

As mentioned above, to find the δ from parameters \mathbf{p} that reduces χ^2 , we iterate starting from \mathbf{p}_0 and take steps in a steepest descent direction δ with $\mathbf{H}(\mathbf{p})$ being positive definite. The iteration procedure is given by Newton Multivariate Method

$$P_{n+1} = P_n - (\nabla^2 \chi^2(\mathbf{p}_n))^+ \nabla \chi^2(\mathbf{p}_n) \quad (4.16)$$

Here is brief outline of the Newton Multivariate Method:

- Start with initial guess parameters for antenna gain factors g_0 and true sky signal s_0 at $n = 0$, $\mathbf{P}_0 = (g_0, s_0)$.
- Iterate to a new step through $\mathbf{P}_{n+1} = \mathbf{P}_n - \alpha(\mathbf{H}(\mathbf{p}_n))^+ \nabla \chi^2(\mathbf{p}_n)$, where α is scaling constant .
- Iterate for N steps until $\chi^2(\mathbf{P}_n) \leq \epsilon$, where ϵ is the required minimum χ^2 .

We provide a reference Python implementation available from github, located at this site ¹. We call this code `lincal` and it should produce the same results as linear redundant calibration discussed in (Liu et al., 2010).

4.3.1 Gradient and Curvature Test

In this section, we briefly discuss gradient and the curvature test of χ^2 in Equation 4.10. To perform a gradient test to χ^2 , we Taylor expand χ^2 it to first order around point X_0 :

¹<https://github.com/Mdlalose/lincal>

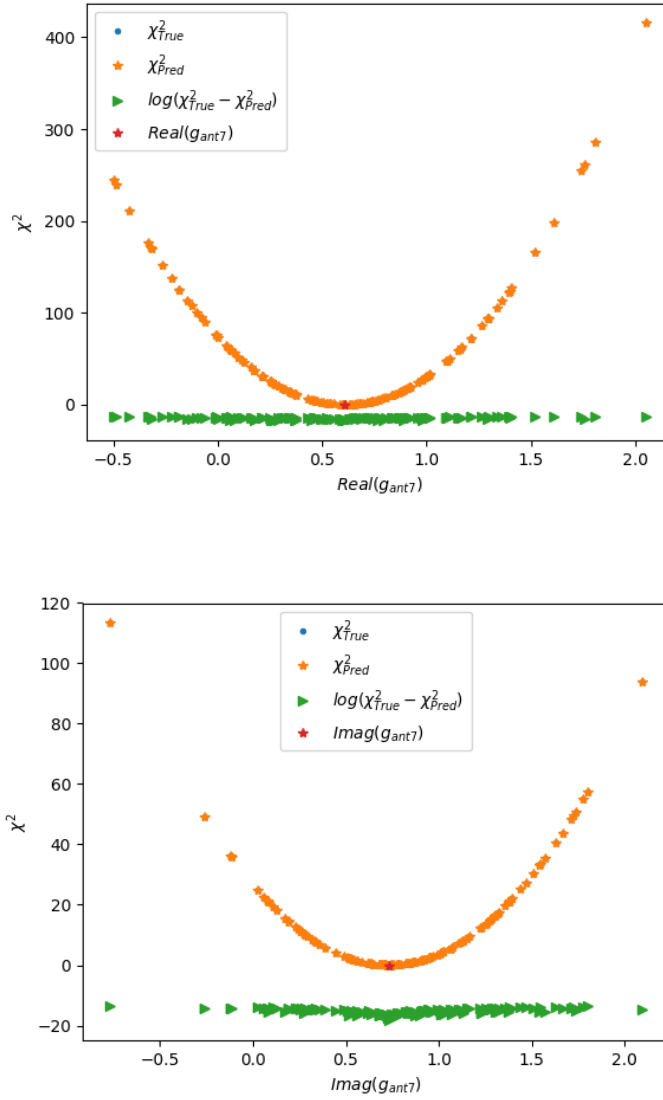


Figure 4.2: A Plot of χ^2 true, χ^2 predicted from second-order approximation and residuals between true and predicted χ^2 for both real and imaginary part of antenna gain. From the two above plots the second-order approximation of χ^2 predict true χ^2 when we vary one parameter, antenna gain (ant7), fixing other parameters. The size of residuals between true and predicted χ^2 are 10^{-20} .

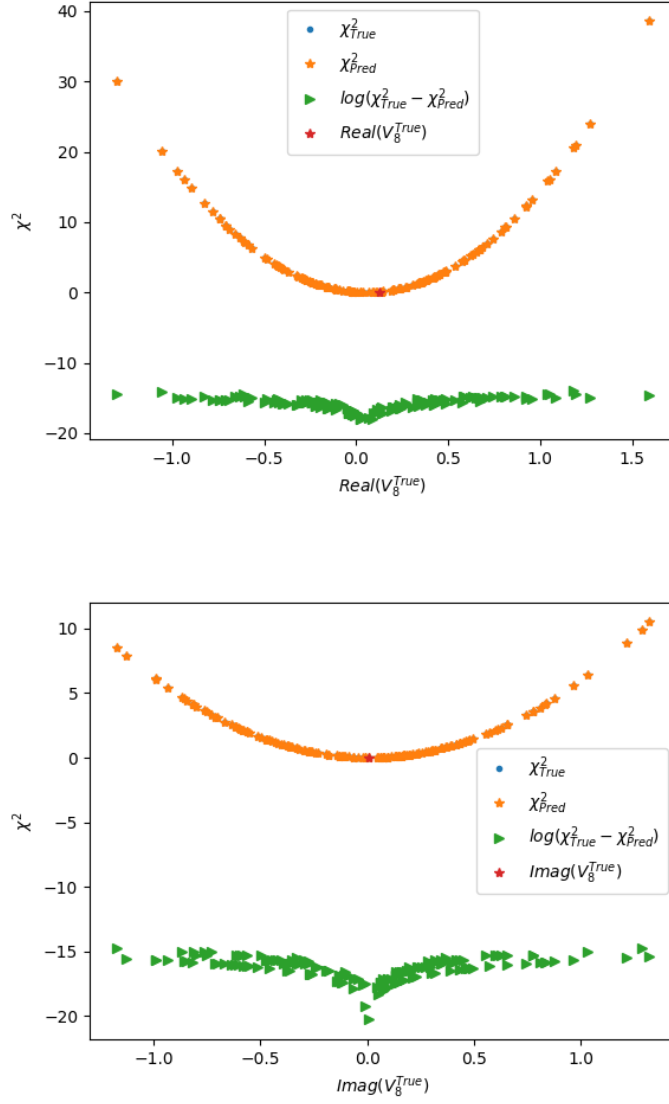


Figure 4.3: A Plot of χ^2 true, χ^2 predicted from second-order approximation and residuals between true and predicted χ^2 (log scale) for both real (top) and imaginary (bottom) part of true visibility. From the two above plots the second-order approximation of χ^2 predict true χ^2 when we vary one parameter, a true sky visibility V_8 (from an 8th set of unique true sky visibility) , fixing other parameters. The size of residuals between true and predicted χ^2 are about 10^{-20} .

$$\chi^2 \approx \chi_0^2 + (X - X_0) \left(\frac{\partial \chi^2}{\partial X} \right) + O(X^2) \quad (4.17)$$

If we take random steps around $X_0 \in X_0$, say $X = X_0 + \beta$, where β is a random number, then the error residual between χ^2 Equation 4.10 and first-order approximation of χ^2 Equation 4.17 are quadratic, $O(X^2)$ and the minimum point is at x_0 . The linear approximation of χ^2 given by Equation 4.17 is tangent χ^2 at X_0 .

To test the curvature, we approximate χ^2 to second-order around X_0 :

$$\chi^2 \approx \chi_0^2 + (X - X_0) \left(\frac{\partial \chi^2}{\partial X} \right) + (X - X_0)^T \left(\frac{\partial^2 \chi^2}{\partial X^2} \right) (X - X_0) + O(X^3) \quad (4.18)$$

Note that the χ^2 second-order approximation at a critical point X_0 , $\frac{\partial \chi^2}{\partial X_0} = 0$,

$$\chi^2 \approx \chi_0^2 + (X - X_0)^T \left(\frac{\partial^2 \chi^2}{\partial X^2} \right) (X - X_0) + O(X^3) \quad (4.19)$$

In the second-order approximation, the curvature of χ^2 captures all the relevant information about the shape of χ^2 in a local neighbourhood. If again we take random steps around $x_0 \in X_0$, χ^2 is quadratic x_0 and it can be predicted using first-order approximation and second-order approximation of χ^2 . Figures 4.2 and 4.3 displays the plots of true χ^2 and the predicted χ^2 using a second-order approximation. We note that predicted χ^2 predict true χ^2 well with residual size are of about 10^{-20} . This shows us that with gradient and curvature of χ^2 in 4.12 and 4.13 we do converge to an optimum solution. In the next section, we present the results from simulations and discussion.

4.4 Results and Discussion

A case study on the calibration requirement to detect 21 cm EoR power spectrum, shows that 1 part to 10^3 calibration errors due to the incompleteness in the calibration source catalogue makes the 21 cm power spectrum measurement impossible (Barry et al., 2016). Different instrumental systematic that lead to same calibration errors will swamp the desired signal. In this analysis, we desire to determine the level of calibration errors we get due to variations in antenna's primary

beams. We run redundant baseline calibration code on two cases of simulations: a perfect redundant array and quasi-redundant to 5% variations in antenna's primary beams as observed from HERA antenna gain auto-correlations.

4.4.1 Simulation

We simulate a HERA like 8×8 antenna array, with antennas place at 10 meters apart located at the PAPER site, Karoo South Africa, see Figure 4.4. For computational simplicity, we use Gaussian primary beams with a 7 deg Full-Width-Half-Maximum each. A more realistic antenna primary beam model will be consider in future, we use Gaussian distribution function to model the main lobe with cut off at 8.59 deg. For further simplification, we consider a flat-sky approximation on visibility simulations. However, the results of the analysis are independent of the curvature of the sky. We simulate true sky visibility of a all point sources with position $\hat{\mathbf{s}}$ measured by baseline \mathbf{b}_{i-q} at frequency ν as follows:

$$V^{true}(\mathbf{b}_{i-q}, \nu) = \sum_{\text{all sources}} B(\mathbf{z} \cdot \hat{\mathbf{s}}) F(\hat{\mathbf{s}}) (\nu/\nu_0)^{-\alpha} \exp\left(-2\pi j \left(\frac{\mathbf{b}_{i-q} \cdot \hat{\mathbf{s}}}{\lambda}\right)\right) \quad (4.20)$$

And observed visibility:

$$V^{observed}(\mathbf{b}_{i-q}, \nu) = g_i^*(\nu) g_q(\nu) V^{true}(\mathbf{b}_{i-q}, \nu) \quad (4.21)$$

Gaussian primary beam with a Full-Width-Half-Maximum size $\theta_{FWHM} = 2.35\sigma_{iq}$ and $\sigma_{iq} = \frac{0.5(1.22\lambda)}{D}$;

$$B(\theta) = \exp\left(-\frac{\theta^2}{\sigma^2}\right) \quad (4.22)$$

where θ is given by

$$\theta = \cos^{-1}(\mathbf{z} \cdot \hat{\mathbf{s}}) \quad (4.23)$$

here \mathbf{z} is zenith vector (perpendicular to 8×8 array), $F(\hat{\mathbf{s}})$ is the flux of the point source at position \mathbf{s} in the sky, ν_0 central frequency and α is a source spectral index, $\alpha \sim \mathcal{N}(-0.8 - 3.5)$ at frequencies. g_i^* and g_q antenna gain factor from antenna i and q respectively. Out of 307455 point sources taken from Murchison Widefield Array (MWA) point source catalogue at 170 MHz- 231 MHz frequency (Hurley-Walker et al., 2017); we simulate visibility data with 1877 point sources

that lies within 32 deg^2 field-of-view, we pick a representative phase centre to be at $(21.4278, -30.7224) \text{ deg}$. In this analysis the per-visibility noise $\sigma_{iq} = 1$ is taken to a unit (or a diagonal noise weight matrix $\mathbf{W} = \mathbf{I}$), so that we can determine the calibration errors level with high precision.

A plot on the bottom of Figure 4.4 shows antenna's primary beam pattern as function of the sky position θ .

4.4.2 Calibration Errors for Redundant Array

The true gains g_i^* and g_q are simulated from amplitudes and phases from a uniform distributions $\mathcal{U}(0.1, 1.2)$ and $\mathcal{U}(0.0, \pi)$. The initial guess parameters for both gains and sky visibility are offset by 20% scatter from true parameter values.

In practice the logarithm calibration solution are taken as initial guess for linear redundant baseline calibration algorithm. Here we take an arbitrary 20% offset scatter from the true solution. In this work, we use Newton Multivariate minimization method to converge to the minimum point and the results should be the same as linear redundant method implemented in (Liu et al., 2010). Figures 4.5 - 4.6 shows the calibration solution for 170MHz-230MHz with initial guess parameters offset by 20% from true gains and sky visibilities. Here we report gain calibration solution after removing absolute gain and phase gradient degeneracies. To remove absolute amplitude and phase degeneracy, we divide by the absolute of the average gain across all antennas at each frequency. In the absence of the sky information, we set the phase to be zero across the array, by fitting the phase gradient (using 4.9) and subtracting the fitted phases from the phase calibration solutions. With same cut-off value of $\chi^2 = 10^{-20}$, an optimum calibration solution is reached after 10 iterations with an average gain amplitude/phase calibration error across all antennas and frequency, 0.5×10^{-11} and 0.13×10^{-11} respectively. From the above analysis, we can conclude that lincal is able to give calibration solution within few iterations (five-ten iterations) with the calibration errors below the EoR signal detection requirement. In the following sections we will look at how the lincal performance in the case of simulations with 5% variations in antenna's primary beams.

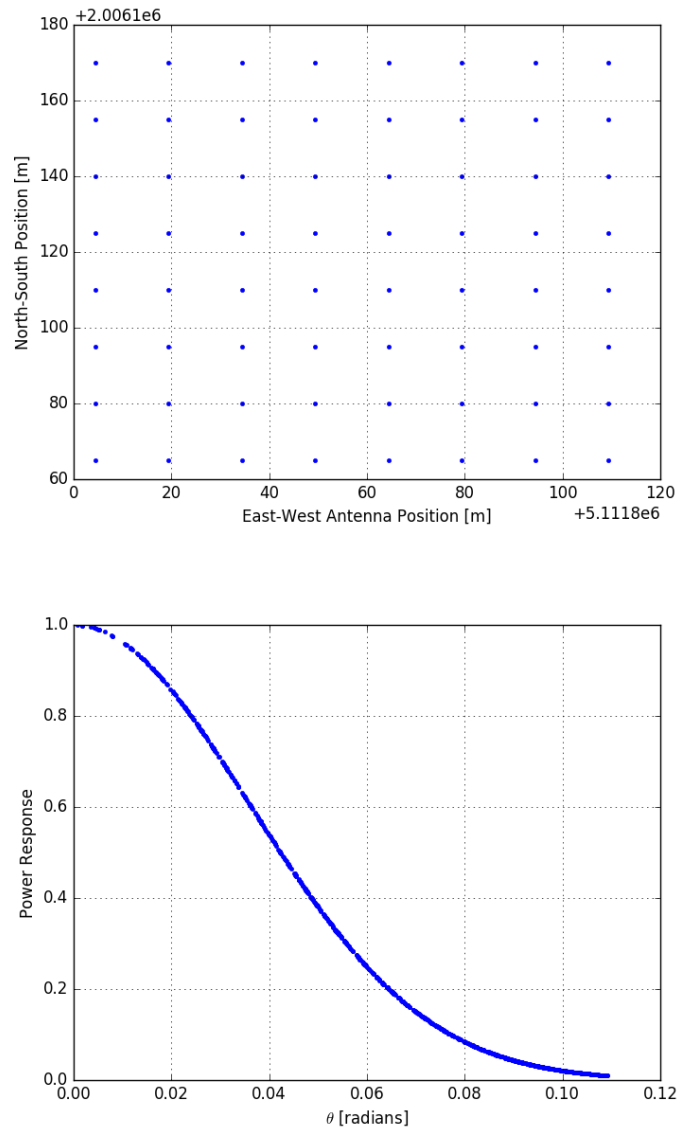


Figure 4.4: *Top:* A 8×8 HERA like antenna array, located at SKA site, Karroo, South Africa. We pick a representative phase centre to be at $(21.4278, -30.7224)$ deg. *Bottom:* Gaussian primary beam pattern with a Full-Width-Half-Maximum of 7 deg.

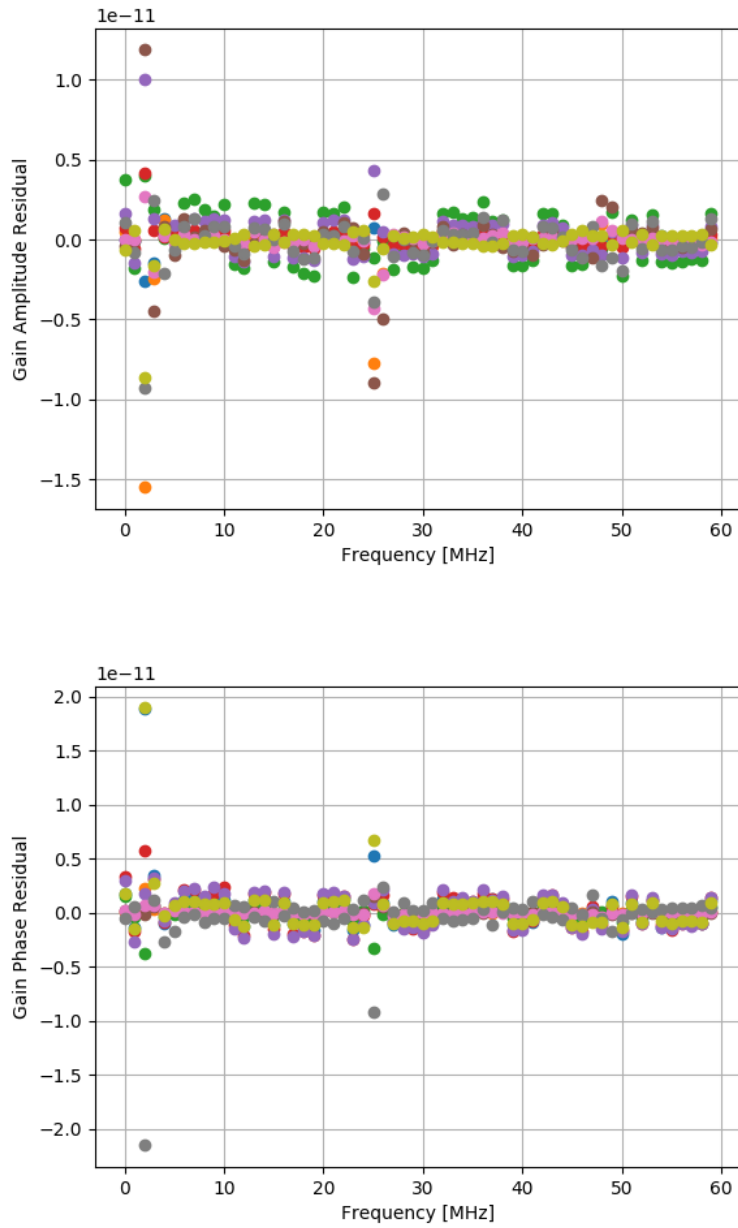


Figure 4.5: *Top* : A scatter plot of antenna gain amplitude residual for 64 antennas at 170-230 MHz. *Bottom* : A scatter plot of phase residual at for all 64 antennas at 170-230 MHz. An optimum solution is reached after 10 iterations with the average amplitude/phase calibration errors across all antennas and frequency, 0.5×10^{-11} and 0.13×10^{-11} respectively. Each colour represents the antenna gain residuals from each individual antenna.

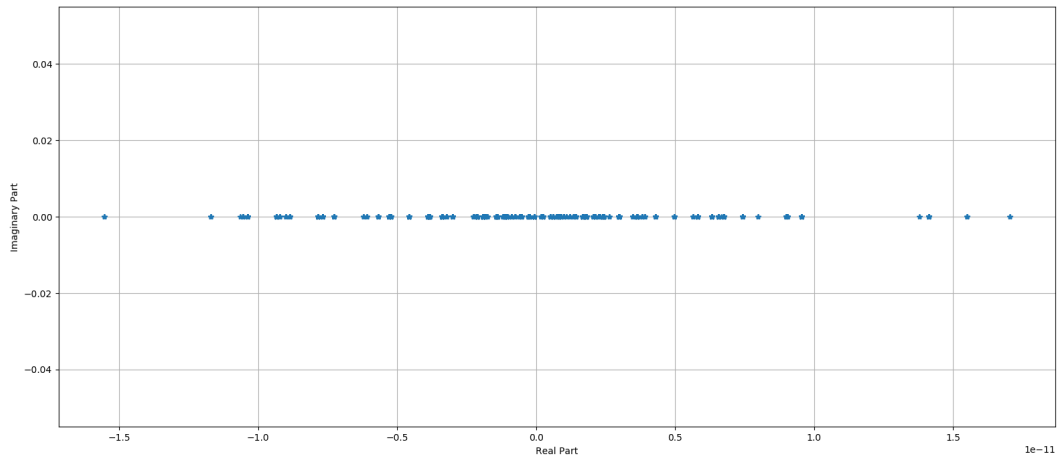
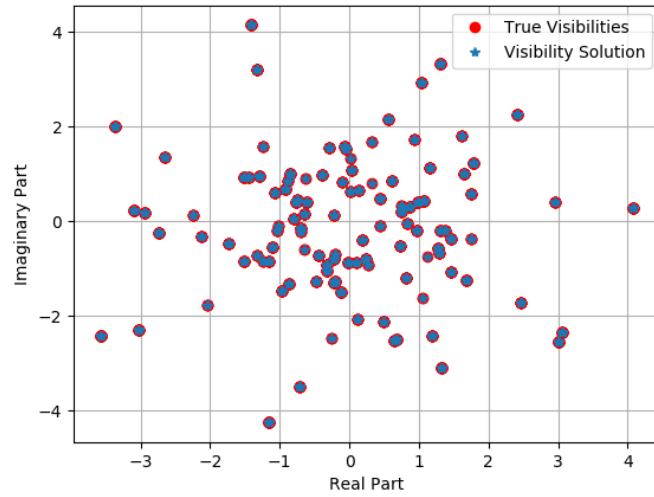


Figure 4.6: *Top*: A plot of true visibilities (red dots) and best fit visibilities (blue stars) on the complex plane at 170 MHz. With a cut-off χ^2 of 10^{-20} , an optimum solution is reached after 10 iterations with significantly small residuals of order 10^{-11} and 10^{-19} for real and imaginary components respectively, see the bottom plot of Figure 5.5.

4.4.3 Quasi-Redundant Array Simulations

In Chapter Four, Equation 4.1, we defined correlations measured by antenna i and q as

$$c_{iq} = g_i^* g_q s_{i-q} + n_{iq} \quad (4.24)$$

where g_i and g_q are antenna gain factors. $s_{i-q} \equiv V_{i-q}$ is true sky visibility seen by baseline $i - q$, and n_{iq} is per-visibility noise associated with measurement V_{i-q} . For a primary beam $B_{iq} = B_i^* B_q$ and sky intensity I , V_{i-q} is defined as:

$$V_{i-q} = \int_{sky} B_{iq} I \exp(-j2\pi \frac{\mathbf{b}_{i-q} \cdot \hat{\mathbf{s}}}{\lambda}) d\Omega \quad (4.25)$$

where \mathbf{b}_{i-q} is baseline vector and $\hat{\mathbf{s}}$ source positions in the sky. In traditional redundant baseline calibration, the key assumption is that the equal baseline with identical primary beam should measure the same sky value. However, in reality imperfections in the array exist, due to either variations in antenna's positions or primary beams.

In this case, we look at the case where B_i and B_q are not identical. Supposed that B_i and B_q are Gaussian primary beam given by:

$$B_i = \exp(-\frac{\theta^2}{2\sigma_i^2}) \quad (4.26)$$

And

$$B_q = \exp(-\frac{\theta^2}{2\sigma_q^2}) \quad (4.27)$$

and $\sigma_i = \sigma_0 * (1 + \epsilon_i)$ and $\sigma_q = \sigma_0(1 + \epsilon_q)$ are antenna's primary beam size (related to Full-Width-Half-Maximum $\theta_{FWHM} = 2\ln\sqrt{2}\sigma_i$ and ϵ_i and ϵ_q beam variations for antenna i and q respectively . If primary beams are identical, then $\sigma_i = \sigma_0$ and $\sigma_q = \sigma_0$. B_{iq} is given by:

$$B_{iq} = \exp\left(-\frac{\theta^2}{2}\left(\frac{1}{\sigma_i^2} + \frac{1}{\sigma_q^2}\right)\right) \quad (4.28)$$

And

$$V_{i-q}'' = \int_{sky} \exp\left(-\frac{\theta^2}{2}\left(\frac{1}{\sigma_i^2} + \frac{1}{\sigma_q^2}\right)\right) I \exp(-j2\pi \frac{\mathbf{b}_{i-q} \cdot \mathbf{s}}{\lambda}) d\Omega \quad (4.29)$$

To determine the impact of quasi-redundant on the calibration solutions recovered by lincal, we simulate the visibility with 5% beam variations observed on the HERA-19 data. Figure 4.7

shows the antenna auto-correlation of three antennas (10,11,73) from HERA19 data. The top plot on Figure 4.7 displays the antenna gain correlation functions at the Galactic Centre for three antennas (10,11,73); one can note that antenna correlation functions are not identical as expected. Similarly, at high latitude the correlation function are not identical. In both observations, there are 5% variations at a scale of 10 MHz. These variations are not from the atmospheric effect or poor calibration solution. These variations might be caused by the cable reflections as the signal moves from antenna to correlators. These ripples might reduce if the antenna gain cross-correlation is taken. In this work, we wish to determine the level of calibration errors due to these 5% beam variations.

Assuming $\sigma_i(\nu)$ from antenna i has correlation function in frequency ν that follows a Gaussian distribution with correlation length of 10 MHz:

$$\langle \sigma_i(\nu)\sigma_i(\nu') \rangle = \exp(-\nu^2/2(10MHz)^2) \quad (4.30)$$

Therefore, $\sigma_i(\nu)$ can be written as

$$\sqrt{\text{Re}(\mathcal{F}(\langle \sigma_i(\nu)\sigma_i'(\nu) \rangle))} \quad (4.31)$$

here \mathcal{F} is Fourier Transform. Henceforth, a fake data, ϵ is generate as

$$\epsilon = 5\% \frac{\mathbf{F}^{-1}(\sigma(\nu))}{\text{standard - deviation}(\sigma_i(\nu))} \quad (4.32)$$

Figure 4.8 on the left show the ϵ as function of frequency for each 64 antennas. A plot on the right of Figure 4.8, shows a product of primary beam response from antenna 1 and 2 in a case of identical beam and a case of 5% beam variation.

We carry a noiseless simulation analysis at 170 MHz -230 MHz with 5% beam variations presented in Figure 4.8. The calibration results, plotted in Figures 4.9 and 4.10, are obtained after 50 iterations with a minimum χ^2 value of 10^{-7} . From Figure 4.9, the amplitude/phase residual are 10^{-3} orders of magnitude. These residuals are highly correlated between frequencies at the scale of 10 MHz. Comparing per-frequency antenna gain calibration solutions from perfect redundant array on Figure 4.5 and quasi-redundant on 4.9 , one can note that introducing 5% beam variations increases both the gain amplitude and phase residuals by 4 – 5 orders of magnitude.

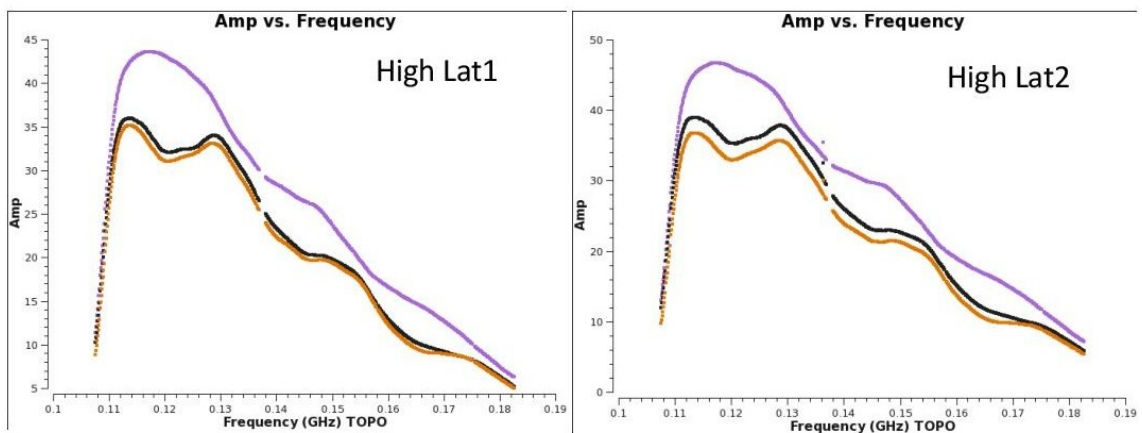
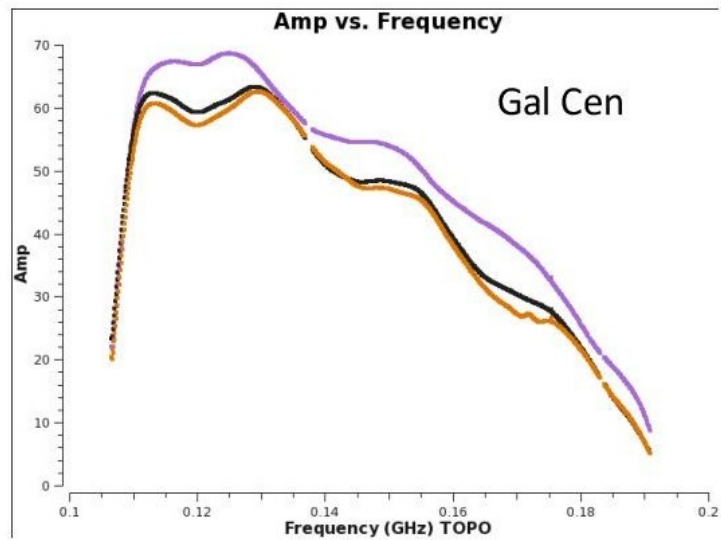


Figure 4.7: *Top*: A plot of gain amplitude auto-correlations as function of frequency for three HERA antennas (10,11,73) at different times . At Galactic Center.*Bottom*: A plot of gain amplitude auto-correlations as function of frequency for three antennas (10,11,73) at high latitude. Data is from HERA19, [courtesy of HERA/Christ Carilli].

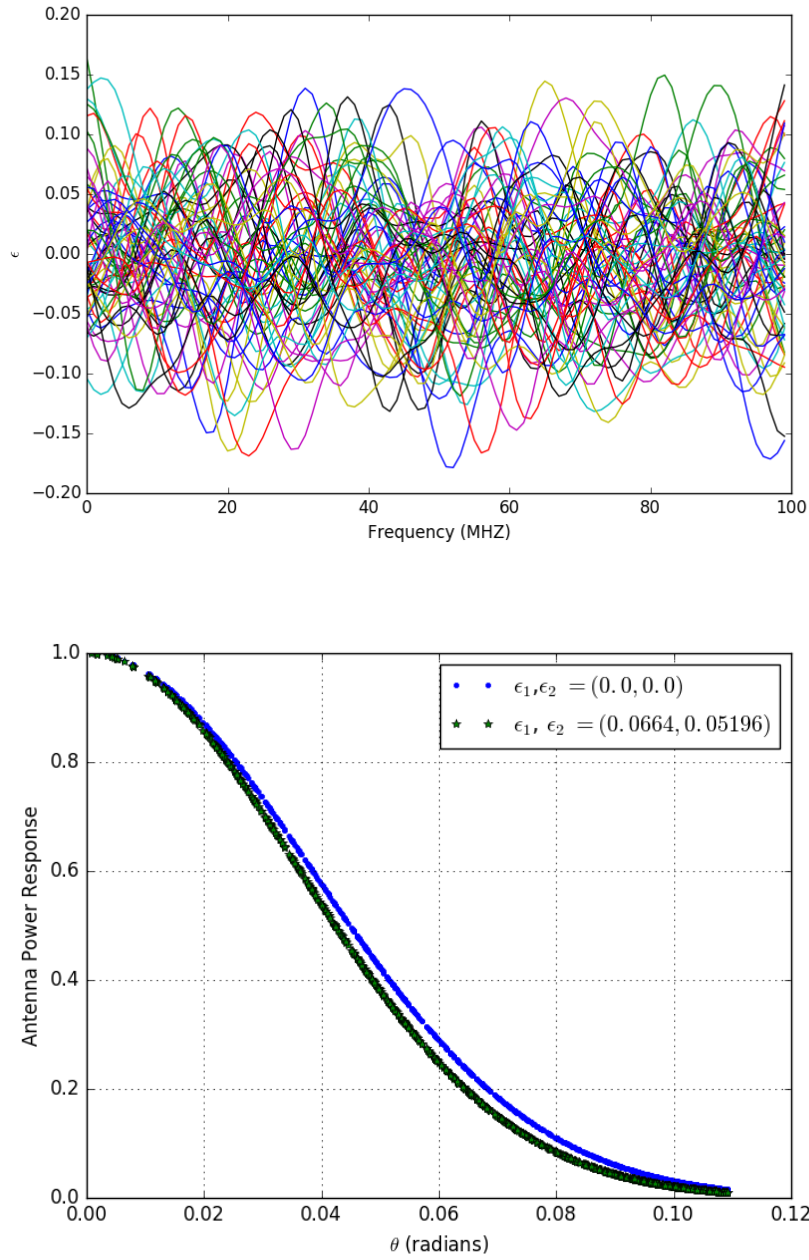


Figure 4.8: *Top*: A plot of ϵ as function of frequency for all 64 antennas. Here ϵ is primary beam variation. *Bottom*: A plot of a product of beam responses from antenna 1 and 2 as function θ in radians for i) identical primary beams, $\epsilon_1 = \epsilon_2 = 0$ (blue curve) and , ii) $\epsilon_1 = 0.0664$ and $\epsilon_2 = 0.0520$ (green curve). There is significant difference in power response between a case of identical primary and 5% beam variations in range of 0.01 – 0.10 radians.

21 cm signal fluctuate as function of position in the sky and frequency. We expect the calibration errors due to random instrumental systemic to average down as we have longer time integration observations. However, the calibration errors that are due to instrumental systemic that correlated in frequency do not average down with long time integration observation. Figure 4.8 displays calibration errors that are correlated at a frequency scale of about $10MHz$.

To further quantify the calibration errors introduced by antenna's beam variations, we compute gain amplitude and phase auto-correlations at lag k :

$$G(k) = \frac{1}{N-k} \sum_{\nu=1}^{N-k} (G(\nu) - \hat{G})(G(\nu+k) - \hat{G}) \quad (4.33)$$

And

$$\Phi(k) = \frac{1}{N-k} \sum_{\nu=1}^{N-k} (\Phi(\nu) - \hat{\Phi})(\Phi(\nu+k) - \hat{\Phi}) \quad (4.34)$$

where ν is frequency range from 170 MHz - 230 MHz and N is number of antennas. Here \hat{G} and $\hat{\Phi}$ are the average of the gain amplitude and phase calibration solutions respectively. We quantify the calibration error by computing the squared root the auto-correlation function at $k = 0$:

$$E(G) = \sqrt{\frac{1}{N} \sum_{\nu=1}^N (G(\nu) - \hat{G})(G(\nu) - \hat{G})} \quad (4.35)$$

And

$$E(\Phi) = \sqrt{\frac{1}{N} \sum_{\nu=1}^N (\Phi(\nu) - \hat{\Phi})(\Phi(\nu) - \hat{\Phi})} \quad (4.36)$$

A plot from Figures 4.13 and 4.14, shows antenna gain amplitude and phase auto-correlation averaged cross all 64 antennas for perfect redundant array and quasi-redundant. The average antenna gain amplitude and phase calibration errors are 1.6×10^{-2} and 9.5×10^{-3} respectively. These calibration errors will make the 21 cm EoR measurement impossible since they are in order of 1 part 10^3 . Therefore, to reconstruct 21 cm power spectrum, it is essential that we minimize these calibration errors. The auto-correlation functions of gain amplitude and phase are correlated up-to about $10MHz$ for 5% beam errors, see Figure 4.13 and 4.14. In the limit of perfect redundancy, we expect the The maximum power of amplitude and phase auto-correlations to be is about 10^{-12} . The maximum amplitude of auto-correlations is larger by about 5-6 orders of

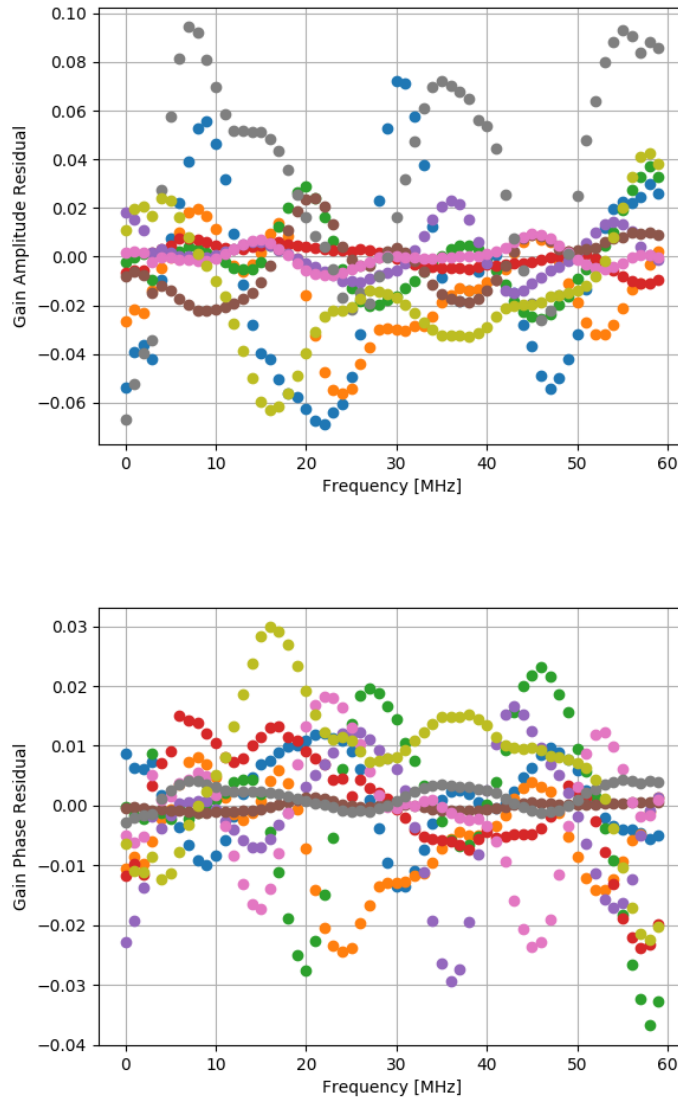


Figure 4.9: *Top*: A plot of gain amplitude calibration solution as functions of frequency. *Bottom*: A plot of gain phase as function frequency. The amplitude/phase calibration errors are $\sim 10^{-2}/10^{-3}$ and highly correlated between frequencies. Each colour represents amplitude/phase residuals for each antenna, with a total of 64 antennas.

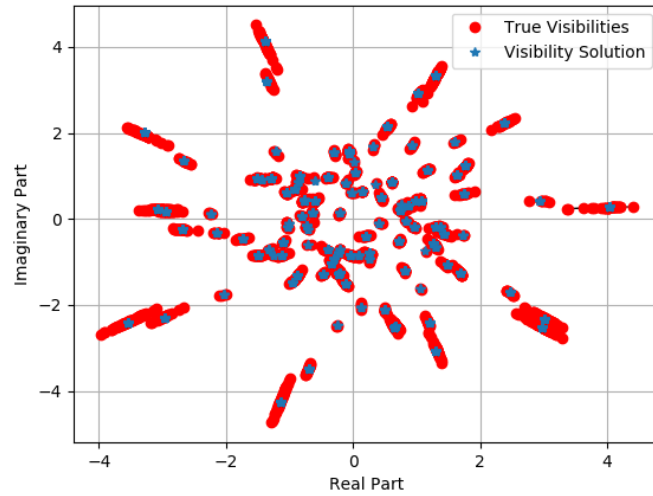


Figure 4.10: A plot of true visibilities (red dots) and best fit visibilities (blue stars) on the complex plane at 170 MHz. With optimum solution after 10 iterations, $\chi^2 = 10^{-20}$

magnitude. From this analysis, one can see that the inability of redundant baseline calibration to account for the quasi-redundant in an antenna array introduces per-frequency antenna calibration errors of same order of magnitude as the desired 21 cm signal. Therefore, now the objective is to reduce these calibration errors by including the information about the variations due to antenna's primary beams and sky in χ^2 minimization process. In the next Chapter, we briefly review correlation calibration scheme (corrcal) that takes into account the instrumental imperfections and the statistical sky information in χ^2 minimization.

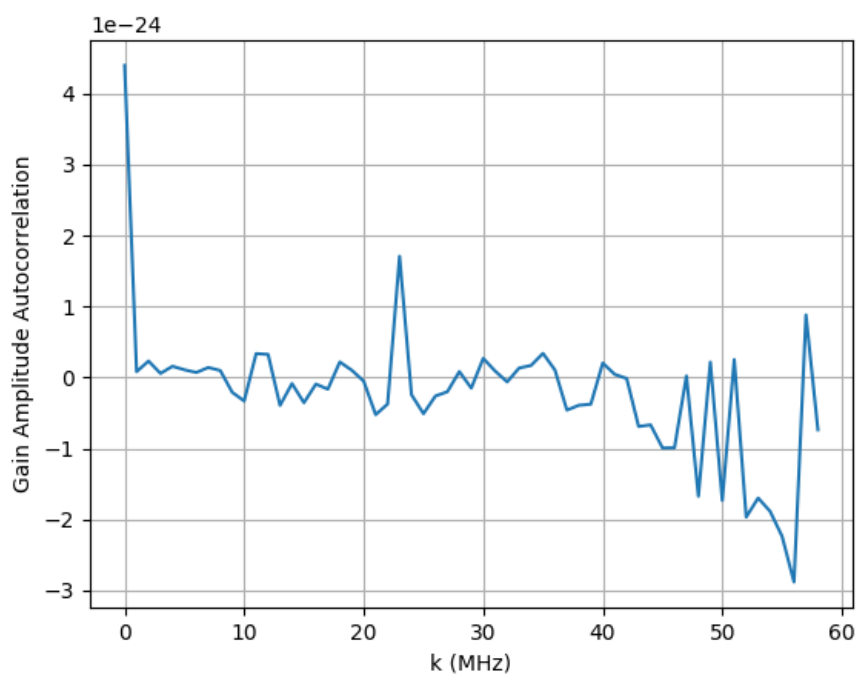


Figure 4.11: A plot of gain amplitude auto-correlation as functions of frequency. At optimum solution amplitude calibration error is 3.7×10^{-12} .

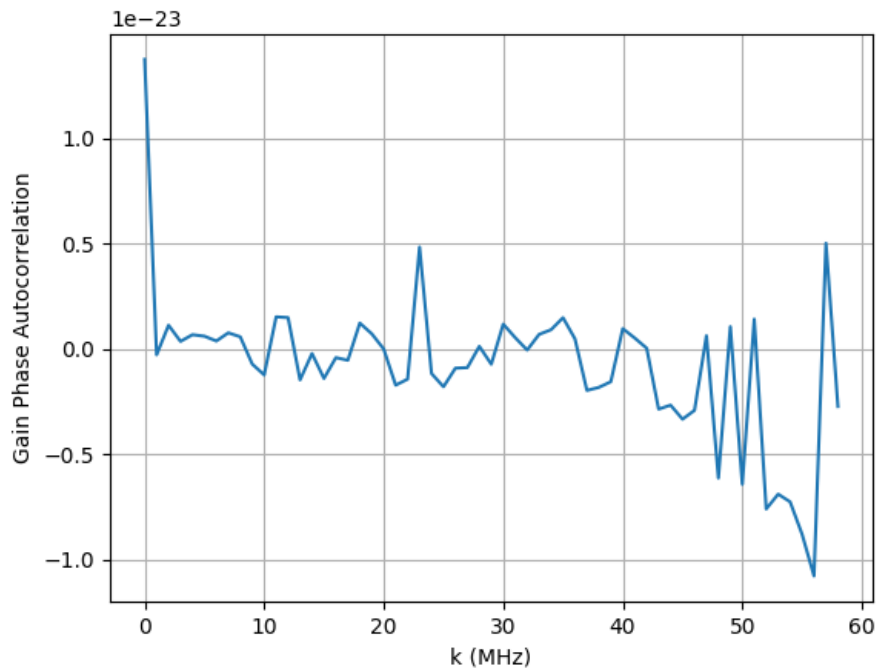


Figure 4.12: A plot of gain phase auto-correlation as functions of frequency. At optimum solution amplitude calibration error is 2.2×10^{-12} .

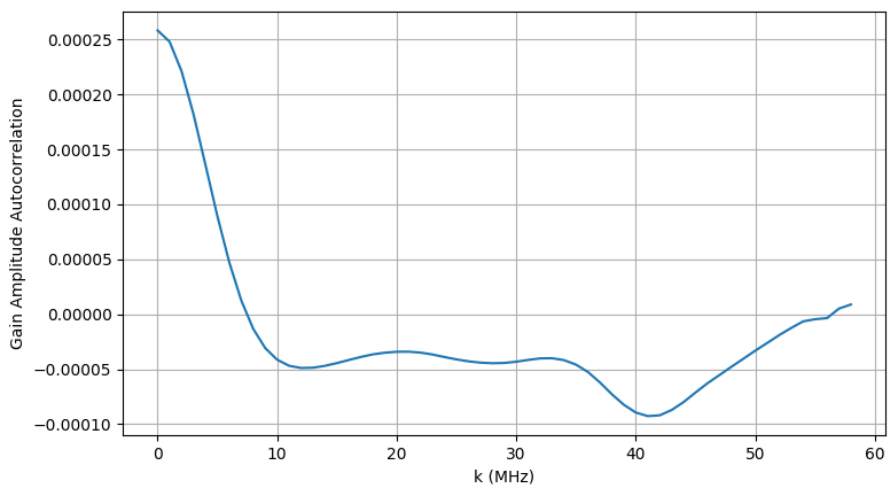


Figure 4.13: A plot of gain amplitude auto-correlation as functions of frequency. At optimum solution amplitude calibration error is 1.6×10^{-2} .

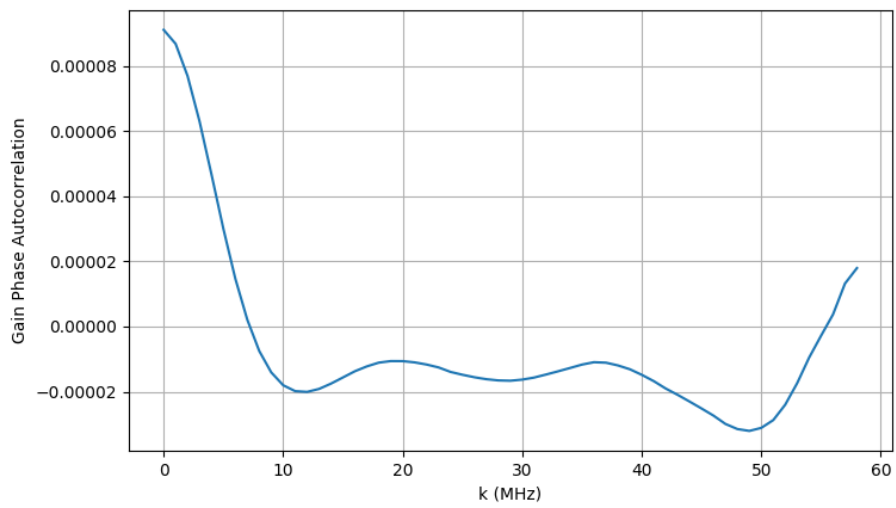


Figure 4.14: A plot of gain phase auto-correlation as functions of frequency. At optimum solution amplitude calibration error is 9.5×10^{-3} .

5.1 Introduction

We saw in the last chapter that ignoring antenna's primary beam variations in redundant calibration analysis produce per-frequency calibration errors that can make the EoR signal detection impossible. In this chapter, we focus on reducing these calibration errors using the correlation calibration formalism presented in Sievers (2017). Consider a measured visibility by baseline \mathbf{b}_{i-q} from antenna i and q :

$$V(\mathbf{b}_{i-q}) = g_i^* g_q \int_{sky} B_{iq}(\theta) I(\theta) \exp(-j2\pi \frac{\mathbf{b}_{i-q} \cdot \theta}{\lambda}) d^2\theta \quad (5.1)$$

where $I(\theta)$ is the intensity of the sky signal from θ direction and $B_{iq}(\theta) = B_i^*(\theta) B_q(\theta)$ is product of the primary beam electric field responses from antenna i and q . Supposed now we define the perceive sky $I(\tilde{\theta}) = B_{iq}(\theta) I(\theta)$ and writing this terms of Fourier Transform;

$$I(\tilde{\theta}) = \int I(\tilde{\mathbf{k}}) \exp(-j2\pi \mathbf{k} \cdot \theta) d^2\mathbf{k} \quad (5.2)$$

Inserting this into Equation 5.1, we get

$$V(\mathbf{b}_{i-q}) = g_i^* g_q I(\mathbf{b}_{i-q}/\lambda) \quad (5.3)$$

In traditional redundant baseline calibration, the key assumption is that the same baseline with identical antenna primary beams measures the same sky value. Assuming uncorrelated noise between visibilities, the form of χ^2

$$\chi^2 = \sum_{i,q} \left(\frac{v_{iq} - g_i^* g_q s_{i-q}}{\sigma_{iq}} \right)^2 \quad (5.4)$$

A gain and sky visibility solutions are obtained by minimizing χ^2 as described in section 4.3. With enough number of unique baselines such that the number of visibilities much greater than the number of antennas plus the number of unique baselines, the solution is determined. However, traditional redundant schemes suffers from four degeneracies; the overall gain amplitude and the global phase. The phase gradient due to the shift in x-direction and y-direction of antennas and the rotation of the sky is indistinguishable from each other and thus resulting into a phase gradient degeneracy. In the following section, we review a correlation calibration method.

We consider a simplistic case where antenna primary beams are Gaussian and a co-planar array. Perfect redundant assumption holds: i) if the baselines deviations $\delta \mathbf{b}_{i-q} = \mathbf{b}_0^k - \mathbf{b}_{i-q} = 0$, where \mathbf{b}_0^k is a single baseline for a redundant set k (for a large array, k run from 1 to $N_{ants}(N_{ants} - 1)/2$) and, ii) if $\sigma_i = \sigma_q$, where $\sigma_i = \sigma_0 * (1 + \epsilon_i)$ and $\sigma_q = \sigma_0(1 + \epsilon_q)$, then $\epsilon_i = \epsilon_q = 0$. The question becomes; how do we calibrate quasi-redundant array due to $\delta \mathbf{b}_{i-q}$ and (ϵ_i, ϵ_q) variations? The proposed idea from Liu et al. (2010), is to fit for gradients in UV-space due to these variations in each redundant block. In Liu et al. (2010) to account for the quasi-redundant due position errors, $\tilde{I}(\mathbf{b}_{i-q}/\lambda)$ in Equation 5.3 is approximated by a First order Taylor expansion:

$$V(\mathbf{b}_{i-q}) = g_i^* g_q \left[I\left(\frac{\mathbf{b}_0^k}{\lambda}\right) + \nabla_{\mathbf{u}} I\left(\frac{\mathbf{b}_{i-q}}{\lambda}\right) \Big|_{\mathbf{b}=\mathbf{b}_0^k} \cdot \frac{\delta \mathbf{b}_{i-q}}{\lambda} \right] \quad (5.5)$$

where $\nabla_{\mathbf{u}}$ is a two-dimensional gradient in uv-plane. Taking the logarithm of Equation 5.3, for example real part is given by:

$$\ln |V(\mathbf{b}_{i-q})| = \eta_i + \eta_q + \ln |c_0^k| + Re(\mathbf{h}_{0u}^k) \ln\left(\frac{\delta \mathbf{b}_{i-q}}{\lambda}\right) + Re(\mathbf{h}_{0v}^k) \ln\left(\frac{\delta \mathbf{b}_{i-q}}{\lambda}\right) \quad (5.6)$$

where $c_0^k \equiv \tilde{I}(\frac{\mathbf{b}_0^k}{\lambda})$, $(\mathbf{h}_{0u}^k) = \nabla_u \ln(\tilde{I})|_{\mathbf{b}=\mathbf{b}_0^k}$ ($\mathbf{h}_{0v}^k) = \nabla_v \ln \tilde{I}|_{\mathbf{b}=\mathbf{b}_0^k}$. A calibration can be performed by solving for \mathbf{h}_0^k and c_0^k simultaneous with antenna gain parameters. However, there are two main problems with this approach: i) Not all the variations can be described as the gradient in uv-plane. For instead, if the beams are getting bigger/smaller as the function of frequency due to variations in antenna's primary beams, that is not gradient type operation. However, it is true that the misplacement of antenna's positions can be described as gradient type operation in uv-plane. To overcome this problem, we need a better description of what the variations will look like and which variations will be big or small. The alternative approach is to weight the observed visibilities by the expected covariance of baselines in each redundant block. Quantitatively, we need to compute the size of the errors due to antenna's primary beam variations and add as noise in noise covariance matrix. The calibration scheme that use visibility covariance to obtain calibration solution is called correlation calibration (Sievers, 2017). In the next section, we briefly review correlation calibration formulation.

5.2 Correlation Calibration

In this section, we briefly review a new calibration scheme that has the benefits of traditional redundant calibration while also allows the inclusion of more realistic models for the instrument and sky. Furthermore, we will show that traditional redundant calibration is one limit case for correlation calibration as discussed in Sievers (2017). We briefly discuss correlation calibration formulation developed in Sievers (2017). Removing the explicit dependency on sky from the redundant baseline calibration scheme is one of the key steps in correlation calibration formalism. In traditional redundant calibration if gains solutions are given, one can easily solve for the sky values V_{iq}^{true} by computing $\frac{V_{iq}}{g_i^* g_q}$ at every UV point. If we assume that all calibrated visibility in a redundant block have the same per-visibility noise σ_k , then the best fit sky estimate is

$$\hat{v}_k = \frac{1}{n} \sum_i v_i \quad (5.7)$$

where n is a total number of visibility within a redundant block . Hence, the χ^2 corresponding to the best sky estimate \hat{v}_k is

$$\begin{aligned}
\chi^2 &= \sum_i \frac{(v_i - \hat{v}_k)^2}{\sigma_k^2} \\
&= \sum_i \frac{(v_i^2 - 2v_i\hat{v}_k + \hat{v}_k^2)}{\sigma_k^2} \\
&= \sum_i \frac{v_i^2}{\sigma_k^2} - 2 \frac{\sum_i v_i \hat{v}_k}{\sigma_k^2} + \frac{\sum_i \hat{v}_k^2}{\sigma_k^2} \\
&= \sum_i \frac{v_i^2}{\sigma_k^2} - 2 \frac{n\hat{v}_k \hat{v}_k}{\sigma_k^2} + \frac{n\hat{v}_k^2}{\sigma_k^2} \\
&= \sum_i \frac{v_i^2}{\sigma_k^2} - \frac{n\hat{v}_k \hat{v}_k}{\sigma_k^2}
\end{aligned} \tag{5.8}$$

where in the cross-term we use $\hat{v}_k n = \sum_i v_i$. An alternative approach is to compute the covariance between two visibilities, $\langle V_p^* V_f \rangle = \alpha^* \alpha$, and add them to a per-visibility noise matrix N_{vis} , where α is sky value measure a set of all redundant baselines. In the case of zero expectation in the measured signal and in the presence of noise correlated between visibilities, χ^2 is

$$v^\dagger N^{-1} v \tag{5.9}$$

where N is an effective noise, a sum of a diagonal per-visibility noise matrix N_{vis} and the sky covariance, an outer product of the vector α times a vector of ones with itself:

$$\mathbf{N} = \mathbf{N}_{vis} + (\alpha \mathbf{1})^\dagger \alpha \mathbf{1} \tag{5.10}$$

Where $\mathbf{1}$ is vector of ones. Since we assumed that all visibilities within a redundant block have the same per-visibility noise σ_k , then $\mathbf{N}_{vis} = \sigma_k^2 \mathbf{I}$. To compute the inverse of \mathbf{N} , we use Woodbury identity:

$$\mathbf{N}^{-1} = \sigma_k^{-2} \mathbf{I} - \sigma_k^{-2} \mathbf{I} \mathbf{1} (\alpha^{-2} + \mathbf{1}^\dagger \sigma_k^{-2} \mathbf{I} \mathbf{1})^{-1} \mathbf{1}^\dagger \sigma_k^{-2} \mathbf{I} \tag{5.11}$$

. Hence, the full χ^2 is

$$v^\dagger (\sigma_k^{-2} \mathbf{I} - \sigma_k^{-2} \mathbf{I} \mathbf{1} (\alpha^{-2} + \mathbf{1}^\dagger \sigma_k^{-2} \mathbf{I} \mathbf{1})^{-1} \mathbf{1}^\dagger \sigma_k^{-2} \mathbf{I}) v \tag{5.12}$$

In traditional redundant calibration, any sky value α for a redundant block is equally likely, meaning a best fit sky value can be very large. This is because redundant baseline calibration is sky model independent. Taking the limit where the sky covariance is approaching infinity or where the sky value is very large $\alpha \rightarrow \infty$, χ^2 becomes

$$v^\dagger(\sigma_k^{-2}\mathbf{I} - \sigma_k^{-2}\mathbf{1}\mathbf{1}^\dagger(\mathbf{1}^\dagger\sigma_k^{-2}\mathbf{1})^{-1}\mathbf{1}\sigma_k^{-2}\mathbf{I})v \quad (5.13)$$

Focusing on the middle term,

$$\begin{aligned} \sigma_k^{-2}\mathbf{I} - \sigma_k^{-2}\mathbf{1}\mathbf{1}^\dagger(\mathbf{1}^\dagger\sigma_k^{-2}\mathbf{1})^{-1}\mathbf{1}\sigma_k^{-2}\mathbf{I} \\ = \sigma_k^{-2}\mathbf{I}(\mathbf{I} - \mathbf{1}\mathbf{1}^\dagger(\frac{\sigma_k^2}{n})\mathbf{1}\sigma_k^{-2}\mathbf{I}) \end{aligned} \quad (5.14)$$

where $\mathbf{1}^\dagger\mathbf{1} = n$. Substituting Equation 5.10 back to Equation 5.9, we get

$$\begin{aligned} v^\dagger(\sigma_k^{-2}\mathbf{I}(\mathbf{I} - \mathbf{1}\mathbf{1}^\dagger/n))v \\ = v^\dagger\sigma_k^{-2}v - \sigma_k^{-2}(v^\dagger\mathbf{1})(\mathbf{1}^\dagger v/n) \\ = \frac{1}{\sigma_k^2}v^\dagger v - \frac{1}{\sigma_k^2}n\hat{v}\hat{v} \\ = \sum_i \frac{v_i^2}{\sigma_k^2} - \frac{1}{\sigma_k^2}n\hat{v}\hat{v} \end{aligned} \quad (5.15)$$

where $n\hat{v} \equiv v^\dagger\mathbf{1}$, $\hat{v} \equiv \mathbf{1}^\dagger v$ and $v^\dagger v \equiv \sum_i v_i^2$. Equation 5.11 is identical to expression of χ^2 in Equation 5.4, therefore the two methods are equivalent. In this work example, we have demonstrated that traditional redundant is limit case of correlation calibration. On the next section, we explore correlation calibration in the case of Gaussian Random Field sky.

5.2.1 Correlation of Visibility

As highlighted in previous section, using covariance-based approach in χ^2 minimization allows us to include realistic models of the instrument and sky. Furthermore, this allows us to quantify the errors due to instrument imperfections and to add them as noise in a noise covariance matrix. In order to run correlation calibration (a.k.a corrcal), we need to compute correlation of visibilities. In this section, present a calculation of correlation of visibilities. In Chapter 2, section 2.1,

we expect the visibility between antenna i and q to be

$$V(u, v) = \int \int A_i^*(l, m) A_q(l, m) I(l, m) \exp(-j2\pi(ul + vm)) dl dm \quad (5.16)$$

where u and v are baseline vectors in of wavelength, $I(l, m)$ is the sky intensity (where l and m direction cosine angles), $A_i(l, m)$ and $A_q(l, m)$ are Gaussian primary beams, given by

$$A_i(l, m) = \frac{1}{\sqrt{2\pi\sigma_i^2}} \exp\left(-\frac{(l^2 + m^2)}{2\sigma_i^2}\right) \quad (5.17)$$

And $A_q(l, m)$

$$A_q(l, m) = \frac{1}{\sqrt{2\pi\sigma_q^2}} \exp\left(-\frac{(l^2 + m^2)}{2\sigma_q^2}\right) \quad (5.18)$$

In this calculation, we take antenna's primary beams to be Gaussian because they are analytically in both real and Fourier space. Traditionally, we combine the antenna beams into a single beam $A_{iq}(l, m) = A_i^*(l, m) A_q(l, m)$, that describe the power pattern of the sky response. In this case, $A_{iq}(l, m)$ is

$$\frac{1}{2\pi\sigma_i\sigma_q} \exp(-(l^2 + m^2)/\sigma_{iq}) \quad (5.19)$$

$\sigma_{iq} = \frac{1}{\sigma_i^2} + \frac{1}{\sigma_q^2}$. In Fourier space $V(u, v)$ is rewritten as convolution of Fourier Transform of $A_{iq}(l, m)$ and $I(l, m)$

$$\mathcal{F}(A_{iq}(l, m)) \otimes \mathcal{F}(I(l, m)) \quad (5.20)$$

here $\mathcal{F}(A_{iq}(l, m))$ is given by

$$\exp(-(|\mathbf{u}|^2)/2\tilde{\sigma}_{iq}) \quad (5.21)$$

where $\tilde{\sigma}_{iq} = 1/\pi\sigma_{iq}$ And $\mathcal{F}(I(l, m))$

$$I(|\mathbf{u}|) \quad (5.22)$$

To obtain visibility in Fourier space, we centre the primary beam on baseline spacing \mathbf{b} and integrate over the sky Fourier transform:

$$V(\mathbf{b}) = \int \int \exp(-(|\mathbf{u} - \mathbf{b}|^2)/2\tilde{\sigma}_{iq}) I(|\mathbf{u}|) du^2 \quad (5.23)$$

The correlation of visibilities between baseline \mathbf{b}_α and \mathbf{b}_β , $C_{\alpha\beta} \equiv \langle V^*(\mathbf{b}_\alpha) V(\mathbf{b}_\beta) \rangle$

$$C_{\alpha\beta} = \langle \left(\int \int \exp\left(-\frac{(|\mathbf{u} - \mathbf{b}_\alpha|^2)}{2\tilde{\sigma}_\alpha}\right) I(|\mathbf{u}|) du^2 \right)^* \int \int \exp\left(-\frac{(|\mathbf{u} - \mathbf{b}_\beta|^2)}{\tilde{\sigma}_\beta}\right) I(|\mathbf{u}|) du^2 \rangle \quad (5.24)$$

where iq is replaced by α and β .

Assuming that the sky I is the Gaussian Random Field, then in Fourier space each mode independent. Therefore, different modes \mathbf{u} are uncorrelated. Hence, the expectation of off-diagonal component disappear and the expectation of the variance is the sky power spectrum $S(|\mathbf{u}|) = \langle I(|\mathbf{u}|) * I(|\mathbf{u}|) \rangle$,

$$C_{\alpha\beta} = \int \int \exp\left(-\frac{(|\mathbf{u} - \mathbf{b}_\alpha|^2)}{2\tilde{\sigma}_\alpha}\right) \exp\left(-\frac{(|\mathbf{u} - \mathbf{b}_\beta|^2)}{2\tilde{\sigma}_\beta}\right) S(|\mathbf{u}|) d^2\mathbf{u} \quad (5.25)$$

We consider case where there are imperfections in antenna's positions, that is, antenna's array is perfectly redundant. If the visibility are from the same redundant block, we recentre the beam to the origin such that $\mathbf{u} - \mathbf{b}_\alpha = \mathbf{u}'$ and $\mathbf{u} - \mathbf{b}_\beta = \mathbf{u}'$,

$$C_{\alpha\beta} = \int \int \exp\left(-\tilde{\sigma}_{\alpha\beta} |\mathbf{u}'|^2\right) S(|\mathbf{u}'|) d^2\mathbf{u}' \quad (5.26)$$

where $\tilde{\sigma}_{\alpha\beta} = \frac{1}{2\tilde{\sigma}_\alpha} + \frac{1}{2\tilde{\sigma}_\beta}$. In the case of the sky with point sources, $S(|\mathbf{u}'|) = S_\nu$ is constant for all $|\mathbf{u}'|$ within a frequency ν (the power of poisson sky is flat). Hence, we can factor it out of the integral:

$$C_{\alpha\beta}(\nu) = S_\nu \int \int \exp\left(-\tilde{\sigma}_{\alpha\beta} |\mathbf{u}'|^2\right) d^2\mathbf{u}' \quad (5.27)$$

Let's transform to polar coordinate, $r^2 = |\mathbf{u}'|^2$,

$$C_{\alpha\beta}(\nu) = S_\nu \int_0^{2\pi} \int_0^\infty \exp(-\tilde{\sigma}_{\alpha\beta} r^2) r dr d\theta \quad (5.28)$$

Integrating, we get

$$C_{\alpha\beta}(\nu) = S_\nu \frac{\pi}{\tilde{\sigma}_{\alpha\beta}} \quad (5.29)$$

While S_ν can be calculated directly from the source count and the beam areas, we instead make pure numerical estimate from the correlations primary beam errors and visibilities as follows: The sum is over the correlation of visibilities within redundant block.

$$\hat{S}_\nu = \frac{\sum V_\nu^*(\mathbf{b}_\alpha) V_\nu(\mathbf{b}_\beta)}{\sum \tilde{\sigma}_{\alpha\beta}} \quad (5.30)$$

where $\tilde{\sigma}_{\alpha\beta} = \frac{1}{2\tilde{\sigma}_\alpha} + \frac{1}{2\tilde{\sigma}_\beta}$

5.2.2 χ^2 Minimization

For n-element array, one can solve for antenna gains, G , by minimizing this χ^2

$$\chi^2 = d^\dagger (N + H^\dagger C H)^{-1} d \quad (5.31)$$

where $H = G^{-1}$, C is the expected data covariance and N is noise covariance matrix. We minimize χ^2 using gradient information only and the minimization is performed using conjugate-gradient method, a Python package. In future work, a curvature information shall be incorporated in solving for antenna gain solution. The gradient with respect to antenna gains is

$$\nabla \chi^2 = 2d^T (N + H^\dagger C H)^{-1} d (H'^T C H) (N + H^T C H)^{-1} d \quad (5.32)$$

To simplify the computation of $\nabla \chi^2$, we evaluate this form $p \equiv (N + H^T C H)^{-1} d$ first then $q \equiv C H p$. The simplified form of gradients is

$$\nabla \chi^2 = 2q^T H' p \quad (5.33)$$

. In the next section we explore correlation calibration solutions from simulations with 5% primary beam errors.

5.3 Correlation Calibration Simulations

In this section, we run correlation calibration in 5% beam errors simulation. To run correlation calibration, located at ¹, visibility data with real and imaginary are separated ($[r_1, i_1, r_2, i_2 \dots]$) and grouped according to redundant blocks. The following fields are required: i) The noise variance of visibilities, $N = \mathbf{I}$, ii) Vector that contains the indices that set off the redundant blocks, iii) The vectors describing the sky covariance's within blocks, $C = Q^T Q$ and $Q = v \lambda^{1/2}$, v) Column the per-visibility response to sources with known positions and lastly, vi) Antenna indices grouped according to redundant blocks.

Since we want calibration errors much better than 10^{-3} , since EoR is has a magnitude of $10^{-3} mK$

¹<https://github.com/sievers/corrcal2>

. Therefore, any eigenvalue bigger than 10^{-6} is important. This guided us to set a threshold eigenvalue, $\lambda_{min} = 10^{-8}$ for the number of modes we use to approximate C from $Q = v\lambda^{1/2}$, $\lambda_{min} \leq \lambda$, in each redundant block. With $\lambda_{min} = 10^{-8}$, a maximum of 4 eigenmode are obtained. We could use the whole exact covariance matrix but using only the 4 largest eigenvalues give everything important to 1 part 10^4 . We set noise level to 10^{-7} and start with initial gains offset by 20% from unit for amplitude and phase components. We present results from two cases, i) 5% beam errors without bright point source include into covariance matrix and ii) 5% beam errors with bright point sources with known positions included into covariance matrix. To remove degeneracy in absolute gain, we divide by the absolute average gain at each frequency. Phase gradient degeneracy is removed by fitting gradient across the array and subtracting it off the phase calibration solution. Figure 6.1, shows the antenna gain calibration solution as function of frequency. We present results from two cases, i) 5% beam errors without bright point source include into covariance matrix and ii) 5% beam errors with bright point sources with known positions included into covariance matrix. To remove degeneracy in absolute gain, we divided by the absolute average gain at each frequency. Phase gradient degeneracy is removed by fitting gradient across the array and subtracting it off the phase calibration solution. Figure 5.1 and 5.2, shows the antenna gain calibration solution as function of frequency.

The amplitude/phase standard deviations of the calibration solution without source treatment in covariance are 1.4×10^{-3} and 4.40×10^{-6} . The amplitude/phase standard deviations of the calibration solution with source treatment in covariance are 1.0×10^{-3} and 4.0×10^{-6} . The calibration errors obtained from lincal are 1.6×10^{-2} and 9.5×10^{-3} for amplitude/phase respectively. Without bright sources treatment, correlation calibration improves the calibration errors by a factor of 11.4 and 2159 for amplitude/phase components. The amplitude/phase Calibration errors improved by a factor of 16/2317 for 30 bright point sources treatment.

Figures 5.3 and 5.4, shows the antenna gain amplitude and phase auto-correlation from lincal, corrcal and corrcal with source treatment in covariance. We can note that the gains are correlated between frequencies up to about $k \leq 10\text{MHz}$ for all cases. However, the gain correlation length decreases for both corrcal cases. Figure 5.3, displays the antenna amplitude and phase auto-correlation with y-axis in log scale. It can be seen clearly that applying corrcal to simulations

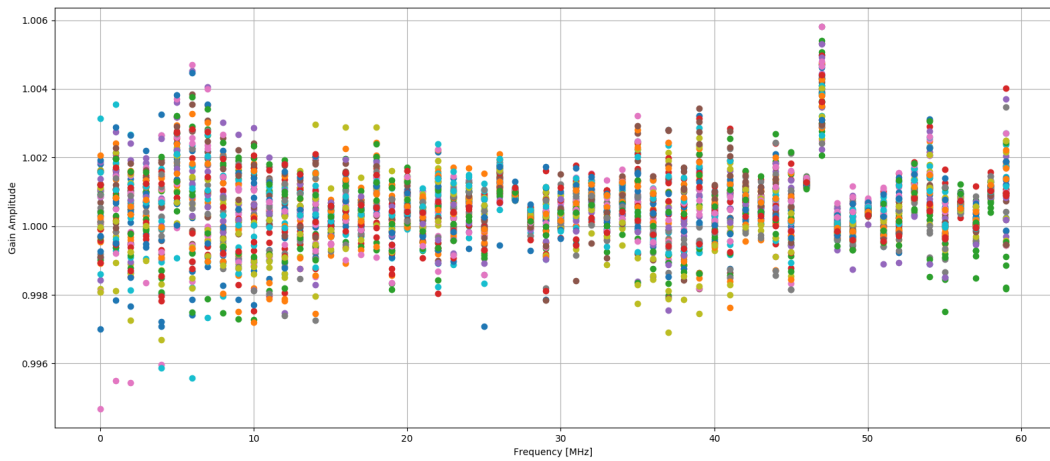
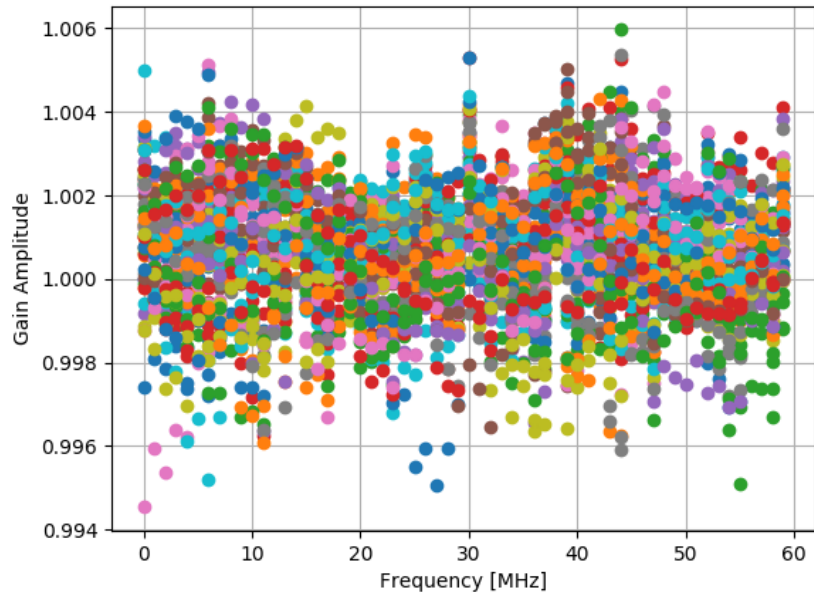


Figure 5.1: *Top*: A plot of gain amplitude calibration solution as functions of frequency without source treatment. *Bottom*: A plot of gain amplitude calibration solution as function frequency. The calibration errors without/with source treatment in covariance are 1.4×10^{-3} and 1.0×10^{-3} .

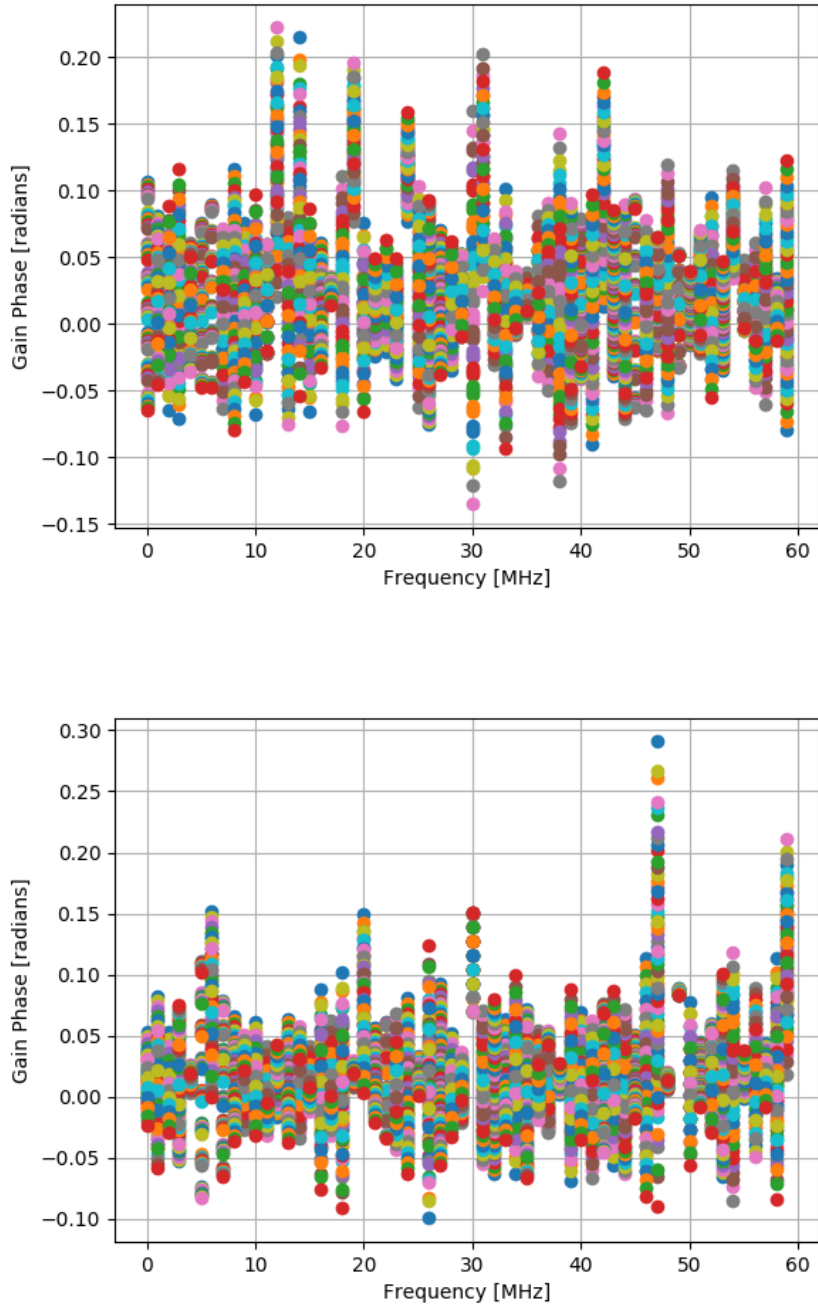


Figure 5.2: *Top*: A plot of gain phase calibration solution as functions of frequency without source treatment. *Bottom*: A plot of gain phase calibration solution as function frequency. The calibration errors without/with source treatment in covariance are 4.40×10^{-6} and 4.0×10^{-6} .

reduces the calibrations errors for both amplitude and phase gain solution. In conclusion, for a 5% variation in antenna's primary beams simulation, using corrcal, we have been being able to significantly reduce amplitude/phase calibration errors by a factor of 16 and 2317 respectively.

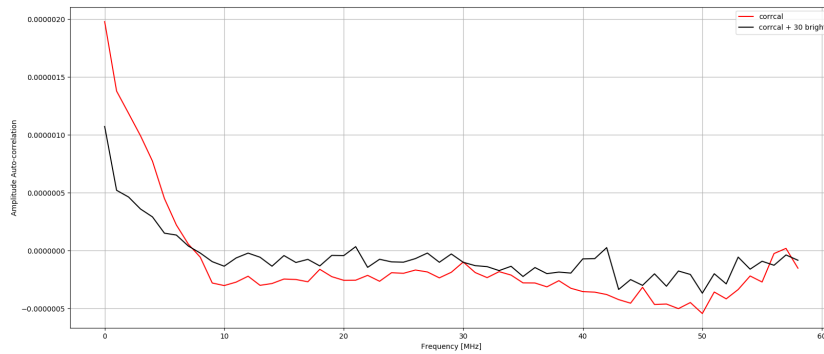
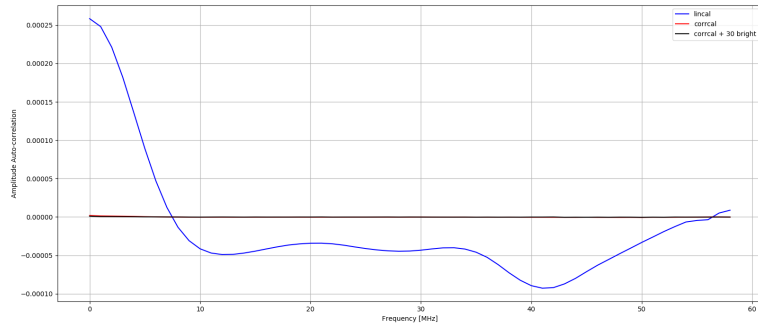


Figure 5.3: *Top*: A plot of lincal (blue curve), corrcal (green curve) and corrcal + bright sources (red curve) gain amplitude auto-correlation as functions of frequency. *Bottom* : A plot of corrcal (green curve) and corrcal + bright sources (red curve) gain amplitude auto-correlation as functions of frequency. Without a bright source treatment, the calibration errors reduced significantly reduced by a factor of 11.4 and for 30 bright source treatment, it improved by a factor of 16.

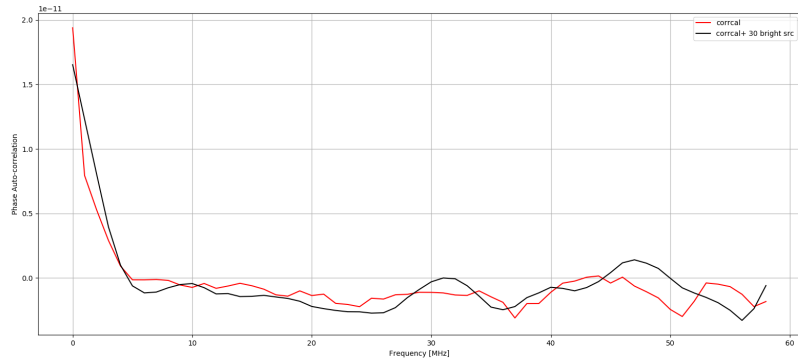
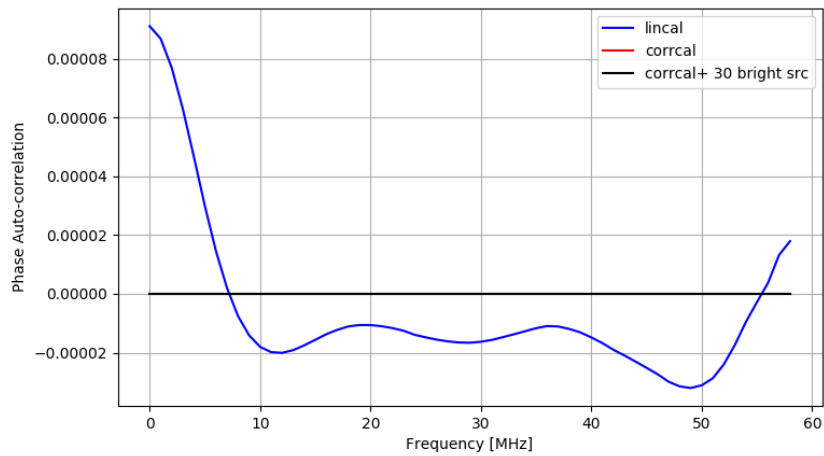


Figure 5.4: *Top*: A plot of linal (blue curve), corrcal (green curve) and corrcal + bright sources (red curve) gain phase auto-correlation as functions of frequency. *Bottom* : A plot of corrcal (green curve) and corrcal + bright sources (red curve) phase auto-correlation as functions of frequency. Without a bright source treatment, the calibration errors reduced significantly reduced by a factor of 2159 and with bright source included, phase calibration errors reduced by 2317

CHAPTER 6

Conclusion

Antenna primary beams variations are common in 21-cm instruments and a high precision calibration is an essential step in EoR power spectrum analysis (Barry et al., 2016). In this work, we have demonstrated that traditional redundant calibration (Liu et al., 2010) in a noiseless case is able to recover exactly redundant simulated data with arbitrarily small calibration errors. However, for a test case of 5% beam errors that was based on observed HERA antenna gain auto-correlations, redundant calibration gives amplitude/phase calibration errors that will swamp the desired 21 cm signal. These findings imply that the inability of traditional redundant calibration to account for array imperfections will present a challenge in calibrating precisely the data from upcoming 21 cm instruments. By relaxing the assumption of perfect redundancy in an array and (optionally) including statistical information about the sky, correlation calibration is able to significantly reduce the calibration errors. We run correlation calibration on the same simulations, and find that correlation calibration improves the amplitude/phase residuals by a factor of 11.4 and 2159 over redundant calibration. By including the position information of just the 30 brightest sources, we have been able to improve the amplitude/phase calibration errors by a factor of 16 and 2317 but the phase calibration only marginally improves. We still have to do more

investigations with more realistic simulations and real data. However, from these simulations results we can conclude that correlation calibration may be able to calibrate imperfect arrays with calibration errors below the 21 cm EoR signal.

In future work, we will consider more realistic primary beams and include the diffuse emission from the Milky Way. We will also extend correlation calibration to take advantage of the spectral smoothness of sources to derive a bandpass calibration. Furthermore, we will explore the impact of quasi-redundancy from 21 cm instruments in EoR power spectrum estimation.

We expect the flexibility of correlation calibration to play a significant role in mitigating the impact of inevitable deviations from redundancy in 21-cm instruments. In principle, correlation calibration can be extended to solve for instrument parameters for 21-cm instruments such as the Hydrogen Epoch of Reionization Array (HERA) (DeBoer et al., 2017), the Hydrogen Intensity and Real-time Analysis eXperiment (HIRAX) (Newburgh et al., 2016), the Canadian Hydrogen Intensity Mapping Experiment (CHIME) (Bandura et al., 2014) and The Tianlai project (Chen, 2012). In the future, once we have incorporated some of these improvements into correlation calibration we will apply it to the real data.

Bibliography

Ali, Z. S., Parsons, A. R., Zheng, H., Pober, J. C., Liu, A., Aguirre, J. E., Bradley, R. F., Bernardi, G., Carilli, C. L., Cheng, C., DeBoer, D. R., Dexter, M. R., Grobbelaar, J., Horrell, J., Jacobs, D. C., Klima, P., MacMahon, D. H. E., Maree, M., Moore, D. F., Razavi, N., Stefan, I. I., Walbrugh, W. P., Walker, A., 2015, 'Paper-64 constraints on reionization: The 21 cm power spectrum at $z = 8.4$ ', *The Astrophysical Journal*, 809 (1), 61.

URL <http://stacks.iop.org/0004-637X/809/i=1/a=61>

Ali, Z. S., Parsons, A. R., Zheng, H., Pober, J. C., Liu, A., Aguirre, J. E., Bradley, R. F., Bernardi, G., Carilli, C. L., Cheng, C., DeBoer, D. R., Dexter, M. R., Grobbelaar, J., Horrell, J., Jacobs, D. C., Klima, P., MacMahon, D. H. E., Maree, M., Moore, D. F., Razavi, N., Stefan, I. I., Walbrugh, W. P., Walker, A., 2015, 'PAPER-64 Constraints on Reionization: The 21 cm Power Spectrum at $z = 8.4$ ', *The Astrophysical Journal*, 809, 61.

Bandura, K., Addison, G. E., Amiri, M., Bond, J. R., Campbell-Wilson, D., Connor, L., Cliche, J.-F., Davis, G., Deng, M., Denman, N., Dobbs, M., Fandino, M., Gibbs, K., Gilbert, A., Halpern, M., Hanna, D., Hincks, A. D., Hinshaw, G., Höfer, C., Klages, P., Landecker, T. L., Masui, K., Mena Parra, J., Newburgh, L. B., Pen, U.-I., Peterson, J. B., Recnik, A., Shaw, J. R., Sigurdson, K., Sitwell, M., Smecher, G., Smegal, R., Vanderlinde, K., Wiebe, D., 2014,

- ‘Canadian Hydrogen Intensity Mapping Experiment (CHIME) pathfinder’, In: *Ground-based and Airborne Telescopes V*, Vol. 9145 of , p. 914522.
- Barry, N., Hazelton, B., Sullivan, I., Morales, M. F., Pober, J. C., 2016, ‘Calibration requirements for detecting the 21 cm epoch of reionization power spectrum and implications for the SKA’, , 461, 3135–3144.
- Carignan, C., Frank, B. S., Hess, K. M., Lucero, D. M., Randriamampandry, T. H., Goedhart, S., Passmoor, S. S., 2013, ‘KAT-7 Science Verification: Using H I Observations of NGC 3109 to Understand its Kinematics and Mass Distribution’, *The Astronomical Journal*, 146, 48.
- Chen, X., 2012, ‘The Tianlai Project: a 21CM Cosmology Experiment’, In: *International Journal of Modern Physics Conference Series*, Vol. 12 of *International Journal of Modern Physics Conference Series*, pp. 256–263.
- Cornwell, T., 1986, ‘Self-Calibration’, *Synthesis imaging*, p. 137 147.
- Cornwell, T., 2004. NINTH SYNTHESIS IMAGING SUMMER SCHOOL self-calibration.
URL <http://www.aoc.nrao.edu/events/synthesis/2004/presentations/Cornwell>
- Cornwell, T., F. Evans, K., 1985, ‘A simple maximum entropy deconvolution algorithm’, 143, 77–83.
- DeBoer, D. R., Parsons, A. R., Aguirre, J. E., Alexander, P., Ali, Z. S., Beardsley, A. P., Bernardi, G., Bowman, J. D., Bradley, R. F., Carilli, C. L., Cheng, C., de Lera Acedo, E., Dillon, J. S., Ewall-Wice, A., Fadana, G., Fagnoni, N., Fritz, R., Furlanetto, S. R., Glendenning, B., Greig, B., Grobbelaar, J., Hazelton, B. J., Hewitt, J. N., Hickish, J., Jacobs, D. C., Julius, A., Kariseb, M., Kohn, S. A., Lekalake, T., Liu, A., Loots, A., MacMahon, D., Malan, L., Malgas, C., Maree, M., Martinot, Z., Mathison, N., Matsetela, E., Mesinger, A., Morales, M. F., Neben, A. R., Patra, N., Pieterse, S., Pober, J. C., Razavi-Ghods, N., Ringuette, J., Robnett, J., Rosie, K., Sell, R., Smith, C., Syce, A., Tegmark, M., Thyagarajan, N., Williams, P. K. G., Zheng, H., 2017, ‘Hydrogen epoch of reionization array (hera)’, *Publications of the Astronomical Society*

of the Pacific, 129 (974), 045001.

URL <http://stacks.iop.org/1538-3873/129/i=974/a=045001>

Field, G. B., 1959, ‘The Spin Temperature of Intergalactic Neutral Hydrogen.’, *The Astrophysical Journal*, 129, 536.

Furlanetto, S. R., Oh, S. P., Briggs, F. H., 2006, ‘Cosmology at low frequencies: The 21 cm transition and the high-redshift Universe’, *Physics Reports*, 433, 181–301.

Högbom, J. A., 1974, ‘Aperture Synthesis with a Non-Regular Distribution of Interferometer Baselines’, , 15, 417.

Hurley-Walker, N., Callingham, J. R., Hancock, P. J., Franzen, T. M. O., Hindson, L., Kapińska, A. D., Morgan, J., Offringa, A. R., Wayth, R. B., Wu, C., Zheng, Q., Murphy, T., Bell, M. E., Dwarakanath, K. S., For, B., Gaensler, B. M., Johnston-Hollitt, M., Lenc, E., Procopio, P., Staveley-Smith, L., Ekers, R., Bowman, J. D., Briggs, F., Cappallo, R. J., Deshpande, A. A., Greenhill, L., Hazelton, B. J., Kaplan, D. L., Lonsdale, C. J., McWhirter, S. R., Mitchell, D. A., Morales, M. F., Morgan, E., Oberoi, D., Ord, S. M., Prabu, T., Shankar, N. U., Srivani, K. S., Subrahmanyam, R., Tingay, S. J., Webster, R. L., Williams, A., Williams, C. L., 2017, ‘GaLactic and Extragalactic All-sky Murchison Widefield Array (GLEAM) survey - I. A low-frequency extragalactic catalogue’, , 464, 1146–1167.

J.P. Hamaker, J.D. Bregman, R. S., 1996, ‘Understanding radio polarimetry: Mathematical foundation’, *Astronomy and Astrophysics Supplement*, v.117, p.137-147.

Liu, A., Tegmark, M., Morrison, S., Lutomirski, A., Zaldarriaga, M., 2010, ‘Precision calibration of radio interferometers using redundant baselines’, , 408, 1029–1050.

Moore, D. F., Aguirre, J. E., Parsons, A. R., Jacobs, D. C., Pober, J. C., 2013, ‘The effects of polarized foregrounds on 21cm epoch of reionization power spectrum measurements’, *The Astrophysical Journal*, 769 (2), 154.

URL <http://stacks.iop.org/0004-637X/769/i=2/a=154>

N. OOZEER, M. B. . S. G., 2014, 'Introduction to casa: A kat-7 data reduction guide', 22–25.

Newburgh, L. B., Bandura, K., Bucher, M. A., Chang, T.-C., Chiang, H. C., Cliche, J. F., Davé, R., Dobbs, M., Clarkson, C., Ganga, K. M., Gogo, T., Gumba, A., Gupta, N., Hilton, M., Johnstone, B., Karastergiou, A., Kunz, M., Lokhorst, D., Maartens, R., Macpherson, S., Mdlalose, M., Moodley, K., Ngwenya, L., Parra, J. M., Peterson, J., Recnik, O., Saliwanchik, B., Santos, M. G., Sievers, J. L., Smirnov, O., Stronkhorst, P., Taylor, R., Vanderlinde, K., Van Vuuren, G., Weltman, A., Witzemann, A., 2016, 'HIRAX: a probe of dark energy and radio transients', In: *Ground-based and Airborne Telescopes VI*, Vol. 9906 of , p. 99065X.

Norman, M. L., 2016, 'From the First Stars and Galaxies to the Epoch of Reionization: 20 Years of Computational Progress', In: *American Astronomical Society Meeting Abstracts*, Vol. 228 of *American Astronomical Society Meeting Abstracts*, p. 305.01.

Pritchard, J. R., Loeb, A., 2012, '21-cm cosmology in 21st century', *Reports on Progress in Physics*, Volume 75, Number 8.

Sievers, J. L., 2017, 'Calibration of Quasi-Redundant Interferometers', *ArXiv e-prints*.